Hindawi
Adsorption Science & Technology
Volume 2022, Article ID 3954536, 24 pages
https://doi.org/10.1155/2022/3954536

Research Article

Study of Barium Adsorption from Aqueous Solutions Using Copper Ferrite and Copper Ferrite/rGO Magnetic Adsorbents

B. Carmel Jeeva Mary,[1] J. Judith Vijaya,[1] M. Bououdina,[2] L. Khezami,[3] A. Modwi,[4] M. Ismail,[4] and Stefano Bellucci[5]

[1]*Catalysis and Nanomaterials Research Laboratory, Department of Chemistry, Loyola College, Chennai 600034, India*
[2]*Department of Mathematics and Science, Faculty of Humanities and Sciences, Prince Sultan University, Riyadh, Saudi Arabia*
[3]*Department of Chemistry, College of Sciences, Imam Muhammad Ibn Saud Islamic University (IMSIU), Riyadh, Saudi Arabia*
[4]*Department of Chemistry, College of Science & Arts at Al-Rass, Qassim University, Saudi Arabia*
[5]*INFN-Laboratori Nazionali di Frascati, Via E. Fermi 54, 00044 Frascati, Italy*

Correspondence should be addressed to J. Judith Vijaya; jjvijaya78@gmail.com

Received 20 May 2022; Revised 25 July 2022; Accepted 24 August 2022; Published 17 September 2022

Academic Editor: Sami-ullah Rather

The development of advanced materials for the removal of heavy metal ions is a never-ending quest of environmental remediation. In this study, a facile and cost-effective approach was employed to synthesize copper ferrite (CF) and copper ferrite/reduced graphene oxide (CG) by microwave assisted combustion method for potential removal of barium ions from aqueous medium. The physiochemical characterizations indicated the formation of magnetic nanocomposite with an average crystallite size of CF and CG is 32.4 and 30.3 nm and with specific surface area of 0.66 and 5.74 m^2/g. The magnetic results possess multidomain microstructures with saturation magnetization of 37.11 and 33.84 emu/g for CF and CG. The adsorption studies prove that upon addition of rGO on the spherical spinel ferrite, the adsorption performance was greatly improved for CG nanocomposite when compared with the bare CF nanoparticles. The proposed magnetic adsorbent demonstrated a relatively high Ba^{2+} adsorption capacity of 161.6 mg·g^{-1} for CG nanocomposite when compared to 86.6 mg·g^{-1} for CF nanoparticles under optimum conditions (pH = 7 ; T = 25°C). The pseudo-first-order (PFO), pseudo-second-order (PSO), and Elovich models were fitted to the kinetic data, the yielded R^2 value of 0.9993 (PSO) for CF and 0.9994 (PSO) for CG which is greater than the other two models, which signify that the adsorption process is chemisorption. Thermodynamic studies show that barium adsorption using CF and CG adsorbents is endothermic. The as-fabricated $CuFe_2O_4$/rGO nanocomposite represents a propitious candidate for the removal of heavy metal ions from aqueous solutions.

1. Introduction

One of the critical challenges faced by the present world is to control the pollution of natural resources, out of which natural water pollution is of primary concern. The direct disposal of heavy metals into the environment by the developed industries is the primary cause of pollution [1]. Heavy metals are nonbiodegradable and therefore accumulate in soil, water, and air which causes serious environmental problems. Hence, the removal of heavy metal from the polluted water is of urgent concern.

Among the heavy metal pollution, barium is the most commonly found radionuclides in industrial wastewater and several other industrial activities such as gas, oil, and petrochemical wastes [2]. In general, barium is soft with white silver metal which easily dissolves in water and thereby readily mobilizes to contaminate the environment [3]. Barium has high fission yield and long half-life which

makes them to form two significant nucleotides of fission products which leads to serious pollution in the environment. This exposure has a detrimental impact on human's health causing various fatal disease [4].

The soluble barium species are considered toxic when compared with insoluble as it stimulates cell processes like paralysis and hypokalemia which results in cardiac attack and respiratory issues. Barium carbonate is strong poison to human because it gets easily dissolved in human stomach. Acute poisoning causes gastrointestinal problems with symptoms like nausea, diarrhea, and gastric pain and neurological problems which causes tremors and mydriasis [5]. Barium also causes musculoskeletal problems with muscle weakness and paralysis effects. Exposure to high doses of barium for a long time leads to chronic poisoning effects which give rise to cardiovascular misfunction and kidney damage in humans. Besides, highly soluble barium chloride is considered more hazardous as it leads to liver and kidney dysfunction, nervous disorders, dyspnea, brain swelling, and paralysis [6, 7].

By considering the toxicity of barium, the World Health Organization (WHO) has regulated the maximum barium concentration of 0.7 mg/L in the clean drinking water [8]. These constraints have prompted special concerns for easy and efficient removal of barium ion pollutant.

The removal of heavy metals by a powerful removal method with easy and new methodology is still a driving concern. Over the recent years, multiple conventional techniques such as electrocoagulation [9], membrane filtration [10], solvent extraction [11], biosorption [12], chemical precipitation [13], ion exchange [14], electrocoagulation [15], cementation [16], and adsorption [17] are being adopted for the removal of heavy metal ions. Many of these techniques have limitations in terms of experimental applicability, operational cost, and removal efficiency. Among these techniques, adsorption is considered one of the most effective and fastest method with significant choice of potential adsorbents used to remove toxic metal ions from waste water [18]. It is also employed to overcome the limitations associated with conventional techniques due to its easy applicability, viability, and effectiveness in the removal of numerous organic and inorganic pollutants [19].

Due to the exceptional features of adsorption technique, several conventional adsorbent materials were developed for the removal of Ba(II) ions from aqueous solution such as biosorbents, conducting polymers, and carbon-based nanocomposites such as carbon nanotube, graphene oxide, and activated carbon [20–23]. Fard et al. [3] prepared MXene by a ball mill process which exhibited adsorption capacity of 9.3 mg/g of Ba(II) within 120 min at pH 6. Majidnia et al. [4] reported that maghemite and titania PVA-alginate beads prepared by a coprecipitation method showed adsorption capacity of 19.37 mg/g of Ba(II) for a contact time of 120 min. Ghaemi et al. [24] suggested that the dolomite powder demonstrated low adsorption capacities of 1.172 mg/g and 3.958 mg/g with a contact time of 120 min at pH 5.5, respectively, for Sr (II) and Ba(II) removal from water. Likewise, Kaveeshwar et al. [25] prepared Pecan shell-based activated carbon by a thermal decomposition method and reported an adsorption capacity of 8.8 mg/g of Sr (II) and 3.3 mg/g of Ba(II) with a longer contact time of 360 min. Torab-Mostaedi et al. [26] reported that commercially perlite exhibited an adsorption capacity of 1.14 mg/g of Sr (II) and 2.49 mg/g Ba(II) for a contact time 90 min at pH 6.

However, it is important to highlight that besides adopting adsorption as an effective method for heavy metal removal, the selection of an appropriate adsorbent to eliminate the pollutant remains crucial. Among the metal oxides, magnetic nanoparticles are reviewed as the most interesting adsorbent materials because of its easy application and removal of heavy metals from waste water [27]. Spinel ferrites are considered excellent adsorbents due to their excellent and controllable magnetic properties, abundance of active sites, and large surface area. This favors adsorption activity by interaction with contaminant ions [28]. Moreover, the magnetic property of spinel ferrites helps in easy recovery of the adsorbent which can be readily washed and reused. The utilization of iron-based nanoparticles as magnetic adsorbents has been widely examined for removal of pollutants from wastewater [29].

Several studies have reported the use of metal ferrite for effective removal of heavy metal ions [30–32]. Among the reported ferrites, copper ferrite ($CuFe_2O_4$) is one of the spinel ferrites that has been identified as a potential candidate for adsorption studies owing to their surface area, catalytic reactions, and excellent magnetic properties [33]. This improved property is due to the tendency of the spinels to occupy the trivalent and divalent cations in octahedral and tetrahedral sites. A comprehensive range of contaminants present in water was removed by copper ferrite. Tran et al. [34] reported that the removal of Pb(II) by Cu-Mg binary ferrite cubical nanoparticles of 30 nm in particle size showed an adsorption capacity of 57.7 mg/g at pH 7. Tu et al. [35] indicated that $CuFe_2O_4$ nanoparticles of particle size 20 to 120 nm exhibited a maximum adsorption capacity of 45.66 mg/g at pH 3.7 for As(III).

However, the low sensitivity of spinel $CuFe_2O_4$ is reformed by graphene-based materials which is enormously applied in the elimination of pollutants. The attention is devoted to graphene oxide-based nanomaterials because of their high surface area, stability, exceptional optical and electrical properties, and high thermal conductivity [36]. Moreover, they are low weight and less toxic and are affordable when compared to other complex organic and inorganic adsorbents [37]. Reduced graphene oxide (rGO) is a two-dimensional structure with a high specific surface area. Hence, in this work, these properties of rGO were exploited on to the surface of spinel copper ferrite to design ferrite-graphene-based nanocomposite for potential adsorbent in barium removal [38].

In the current study, copper ferrite (CF) and copper ferrite-reduced graphene oxide (CG) have been employed for adsorption of Ba(II) ions from aqueous solution. Although many studies on the synthesis of CF and CG nanocomposite using different methods have been reported, their complex methods and the expensive procedures restrict their usage. In this study, CF and CG nanoadsorbents were

synthesized by a microwave-assisted combustion method. It is a commonly used noncontact heating technique for the preparation of nanoparticles which uses dissolved solutions of metal nitrates and fuel to undergo combustion reaction [39]. It is noteworthy that the synthesis of CG nanocomposite can be effectively achieved by a microwave-assisted combustion method [40]. Inside the microwave oven, the microwave energy is converted into heat energy due to strong intermolecular friction which raises the temperature of the sample to undergo rapid exothermic reaction. This results in obtaining pure nanosized particles with better texture, surface area, morphology, and crystallite size in short reaction time [41]. Furthermore, fuel plays a significant role in the combustion process as it oxidizes and thereby liberates CO_2, N_2, and H_2O gases. As a result, the large particles are broken down to smaller particles with the controlled pore size [40]. In recent studies, amino acids are nontoxic inorganic compounds which are regarded as powerful green fuel. They contain free carboxylic and amine functional groups which regulates the surface properties of nanoparticles. In view of its advantages, several studies have used amino acids such as glycine and L-alanine as fuels in a combustion process. L-lysine ($C_6H_{14}N_2O_2$) helps to obtain uniform mixing of reaction mixture, and due to its high flame propagating property, it helps to combust the products [42]. To the best of authors knowledge, preparation of rGO-based copper ferrite nanocomposites using L-lysine as fuel in the microwave-assisted combustion method have not been reported elsewhere.

In the present work, $CuFe_2O_4$ and $CuFe_2O_4$/rGO magnetic nanocomposite was synthesized by the microwave-assisted combustion method using L-Lysine as fuel. The synthesized adsorbents possess increased adsorption sites and are deployed for the removal of Ba(II) ions from aqueous solution. The different adsorption parameters such as pH, contact time, and temperature which influences the removal of Ba(II) ions were examined. In addition, the adsorption efficiency, kinetics, isotherms, and reusability of CF and CG nanoadsorbents were discussed. The possible mechanisms involved on adsorption of Ba(II) ions are studied.

Based on its properties, $CuFe_2O_4$/rGO nanocomposite can be used as an effective adsorbent for the removal of barium ions in the treatment of waste water. Nonetheless, it is important to highlight that there are very limited studies reported in the literature on the removal of barium heavy metal; consequently, there is a necessity of huge demand for new technology development [43]. This study is aimed primarily on the effect of $CuFe_2O_4$ and $CuFe_2O_4$/rGO nanocomposite which is synthesized by the microwave-assisted combustion method using L-lysine (amino acid) as fuel.

2. Experimental Procedure

2.1. Preparation of CF Nanoparticles. CF nanoparticles were synthesized by using copper nitrate hexaferrite ($Cu(NO_3)_2{\cdot}6H_2O$, ≥99%), ferric nitrate nonahydrate ($Fe(NO_3)_3{\cdot}9H_2O$, ≥99%), and L-lysine ($C_6H_{14}N_2O_2$, 99%) which were purchased from Merck and used without any purification. In the current work, a domestic microwave oven was used for the preparation of CF and CG nanocomposite. The nitrate salts of molar ratio of 1 : 2 used as cation precursors were dissolved individually in double distilled water. L-lysine is used as fuel, with the metal nitrate to fuel ratio of 1 : 1. All the solutions were mixed and magnetically stirred to obtain a clear solution. The obtained solution was transferred into a silica crucible and subjected to irradiation in a domestic microwave oven at a frequency of 2.4 GHz with an output power of 850 W for 12 min. The collected black powder was washed thoroughly with distilled water and ethanol.

2.2. Preparation of $CuFe_2O_4$/rGO Nanocomposites. Initially, reduced graphene oxide was prepared using modified Hummer's method [44]. 10 mg of graphene oxide was dispersed in double distilled water to form homogenous solution. To this solution, the prepared 1 : 2 $CuFe_2O_4$ and $Fe(NO_3)_3$ and lysine were added and stirred continuously for 24 h to achieve a homogenous solution. The final solution was transferred to a silica crucible and kept for irradiation in a domestic microwave oven at a frequency of 2.45 GHz, 800 W output power for 10 min. The obtained black precipitate of $CuFe_2O_4$/rGO was thoroughly washed with distilled water and ethanol then dried at 60°C for 8 h.

2.3. Characterization Techniques. The crystal structure of CF and CG samples were checked by X-ray diffraction (XRD) using Bruker D8–Advance diffractometer equipped with Cu-Kα radiation source ($\lambda = 1.5418$ Å). The morphology and the chemical composition of the as-prepared powders were determined by high-resolution scanning electron microscopy (HRSEM) and energy dispersive X-ray spectroscopy (EDS) by means of FEI-Quanta FEG 200F equipped with Zeiss Ultra 55 detectors. Magnetic measurements were carried out at room temperature using vibrating sample magnetometer (VSM) Lake Shore 7404 model equipped with 1.8 Tesla magnet. The surface characteristics of the prepared CF and CG powders were characterized by ASAP 2020 micrometrics analyzer. The structural confirmation and the chemical bonding in the fabricated specimen before and after Ba(II) ion adsorption were identified by means of Fourier transform infrared spectroscopy (FTIR) using the Nicolet 6700 spectrometer. The zero-point (Z_{PC}) was examined by an isoelectric method (IEP). The adsorption of Ba(II) concentration was assessed by means of an ICP Spectro Genesis spectrometer. To study the copper and iron leaching, an atomic absorption spectrometer (PerkinElmer AA-300) was utilized.

2.4. Adsorption Tests. Batch mode adsorption experiments were carried out to optimize the operational conditions and to estimate the adsorption efficiency of Ba(II) ions from aqueous solutions using CF and CG adsorbents. A known stock solution of Ba(II) concentration was dissolved using double distilled water. The initial concentration of Ba(II) ions was 45 mgL^{-1}; 25 mL of Ba(II) ion solution with 10 mg of adsorbent was optimized. The pH of the solution was maintained to be neutral with the addition of 1 M of NaOH. Throughout the experiments, the flasks were shaken at

300 rpm using a mechanical shaker at room temperature for 24 h. At a certain time interval, the supernatant liquid was separated to determine the residual amount of Ba(II) in the aqueous solution.

The removal efficiency and the adsorption capacity (q_e) of CF and CG adsorbent were calculated using the equations given below [38].

$$\% = \left(\frac{C_O - C_e}{C_O}\right) \times 100, \qquad q_e = \frac{V(C_0 - C_e)}{m}, \tag{1}$$

where C_o, C_e, and mg L^{-1} represent the initial and equilibrium concentrations of Ba(II).

q_e is the quantity of the adsorbed Ba(II) per unit mass of adsorbent at a specific time (mg g^{-1}); V is the solution volume (L); m is the mass of the adsorbent (g).

2.5. Adsorbent Stability Test. The stability of CF and CG nanoadsorbents is investigated under various parameters such as water exposure, Ba(II) concentrations, solution pH, and adsorbent reusability. The stability study on the effect of water exposure was examined by direct experiments, in which 0.3 g/L of adsorbents was soaked in ultrapure water for a time duration of 1-5 days. The adsorbents were then dried under air for 70° C to determine the crystalline structure and the adsorption performance of Ba(II). The stability of the solution pH was determined by dispersing 0.3 g/L of the adsorbents in 50 mL of water at pH ranging from 2 to 8 for 24 h. The stability of the nanoadsorbents was examined by using the ICP-OES analyzer.

3. Results and Discussion

3.1. X-Ray Diffraction Analysis. The phase purity and the crystallinity of the prepared CF and CG nanocomposite were determined by using X-ray diffraction [45]. The peaks are substantially sharp which is an indication of the crystalline nature of the prepared samples. The diffractions peaks of CF and CG located at $2\theta = 18.19°$, 30.12°, 35.65°, 37.40°, 39.10°, 43.29°, 57.50°, and 62.78° which are indexed to (111), (220), (311), (202), (222), (400), (511), and (440) planes of the cubic crystal structure of the spinel phase $CuFe_2O_4$ [46]. This is in good match with the JCPDS card number 01-077-0010. However, the XRD pattern of CG reveals low intensity peaks located at $2\theta = 38.9°$, 43.6°, 51.6°, and 63.4°, assigned to the rhombohedral Fe_2O_3 phase which is because of $CuFe_2O_4$ which is well diffused into the GO sheets to stabilize the CF formation [47]. Upon appropriate calcination, the homogeneity of the particle size distribution is achieved during the combustion of the acquired ash with 500°C. The average crystallite of CF and CG nanocomposite was determined using Debye Scherrer's equation [48].

$$D = \frac{0.9\,\lambda}{\beta\,\cos\,\theta}, \tag{2}$$

where D is the crystallite size, λ is the used wavelength, β is the full width at half maximum (FWHM), and θ is the Bragg's diffraction angle. The calculated average crystallite size of CF and CG is 32.4 and 30.3 nm using Debye Scherrer's equation.

Generally, the strong intense diffraction peak at $2\theta = 9.80°$ and a small peak at 42.80° which is indexed to (001) and (002) hkl planes shows the presence of graphite sample [49]. The XRD pattern of CG in Figure 1(a) reveals the absence of diffraction peak of GO, which is due to conversion of GO to rGO during the synthesis of CG nanocomposite. The crystallite size and the microstrain of CF and CG have been calculated using the following methods.

The relatively broadened diffraction peaks in XRD patterns are due to the defects associated with the size and strain in crystal lattice; as a result, the crystallite size calculated from different methods varies. The Williamson-Hall (W-H) method contemplates on the particle size and strain caused in the physically broadened peaks. The investigation of the average crystallite size and the strain caused as a consequence of the distortion in the crystal lattice are analyzed [50]; the integral width of the peak is defined by the following equation [51]:

$$\beta\,\cos\,\theta = \left[\frac{k\lambda}{D}\right] + 4\varepsilon\,\sin\,\theta, \tag{3}$$

where β is the full width half maximum, k is constant (0.9), λ (1.5409 Å) is the wavelength of the X-ray source, D is the crystalline size, and ε is elastic strain. Using this method, CF manifests a crystallite size of 32.3 nm whereas after the addition of rGO it decreases significantly reaching 29.4 nm for CG. This means that rGO inhibits grain growth of $CuFe_2O_4$ crystals during the synthesis process. The determined strain is 0.4% for CF and -4.4% for CG which is expressed in Table 1.

Similarly, the Halder-Wagner (H-W) method deals with the investigation of the strain in the lattice and crystallite size. It is favorable to the small and less intensity and low angle peaks. Moreover, it overcomes the difficulty caused in the W-H method that neglects to agree with the XRD peaks. To simplify the understanding of strain and the crystallite size, the below given expression is used [52]:

$$\left(\frac{\beta^*_{hkl}}{d^*_{hkl}}\right)^2 = \frac{1}{D}\cdot\frac{\beta^*_{hkl}}{{d^*_{hkl}}^2} + \left(\frac{\varepsilon}{2}\right)^2, \tag{4}$$

where $\beta^*_{hkl} = \beta_{hkl}\cdot\cos\,\theta/\lambda$ and $d^*_{hkl} = 2d_{hkl}\cdot\sin\,\theta/\lambda$.

The crystallite size and the microstrain (ε) of CF and CG are listed in Table 1. The calculated crystallite size by the H-W method shows 16.2 nm for CF and 12.5 nm for CG with negligible microstrain values.

It is evident from Table 1 that the crystallite size of CF calculated from H-W and W-H methods shows some variation. This is because the influence of strain on the crystallite size is more significant as well due to the variation of size distribution in CF crystal lattice [53]. In CG, the impact of strain on the crystallite size is negligible; hence, the particle size is similar in both methods. The estimated strain in the W-H method

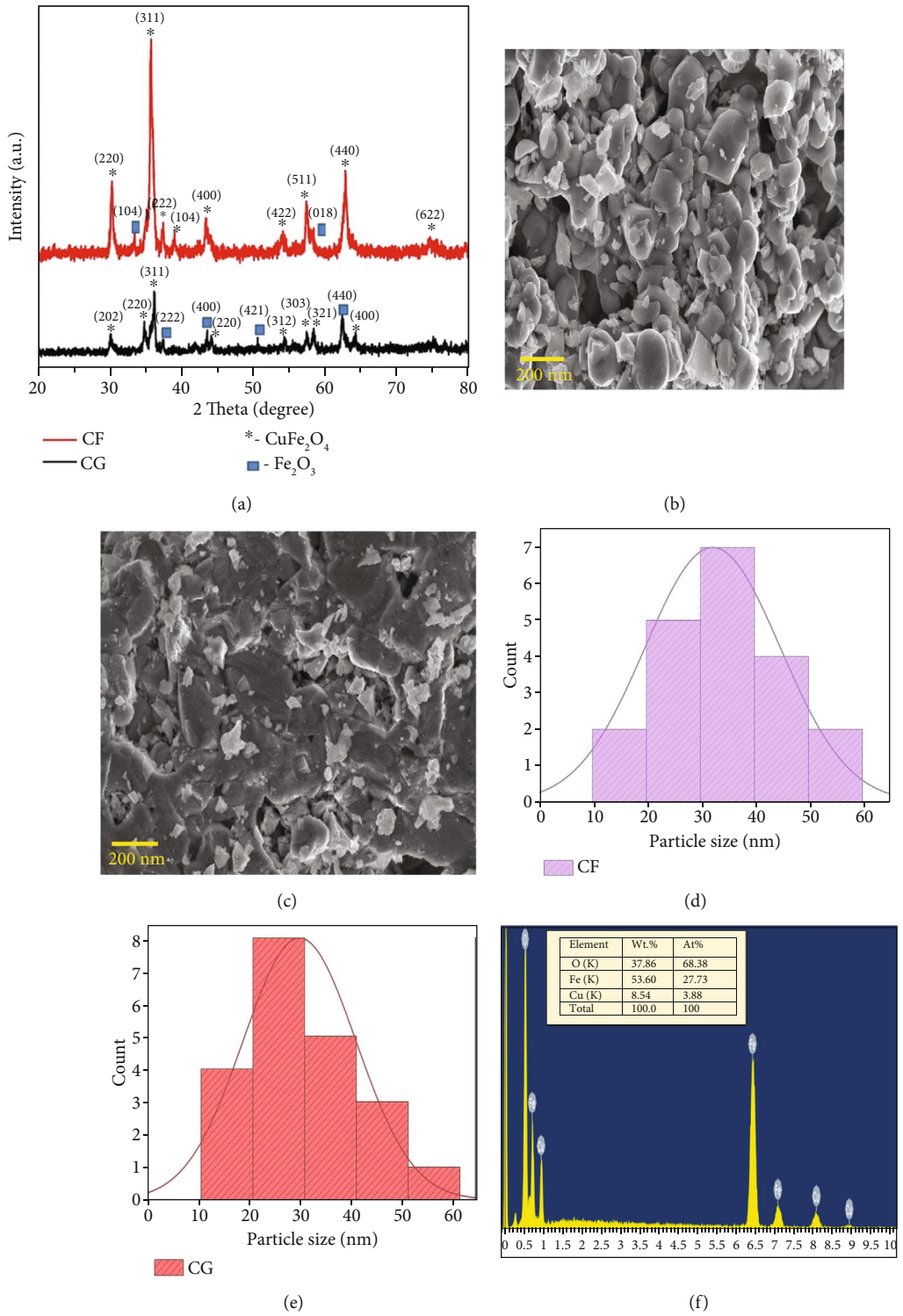

Figure 1: Continued.

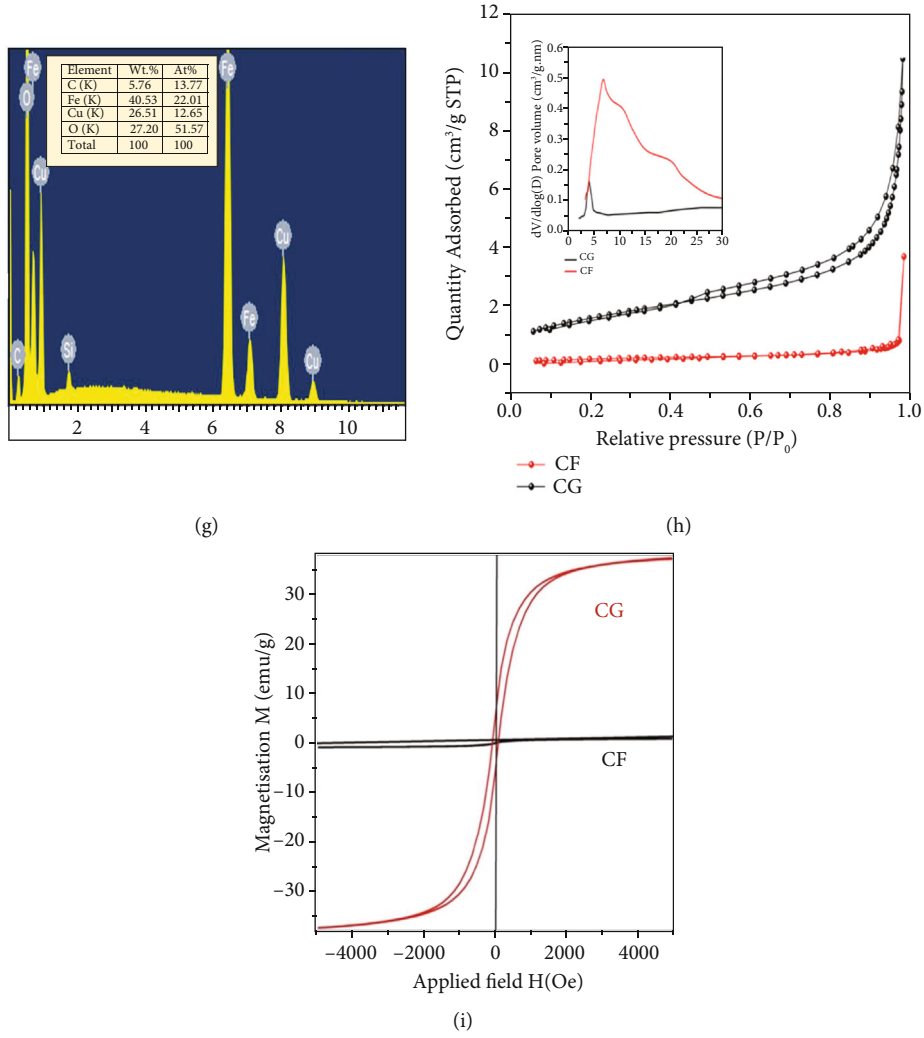

Figure 1: (a) XRD patterns of CF ($CuFe_2O_4$) and $CuFe_2O_4$/rGO (CG); FE-SEM images of (b) CF and (c) CG; the corresponding representative histograms of particle-size distribution with average size calculation by Lorentz fitting of (d) CF and (e) CG; EDX spectra of (f) CF and (g, h) nitrogen adsorption–desorption isotherms of CF and CG nanocomposite; (i) M-H curves recorded at room temperature for CF and CG.

Table 1: Phase composition, structural, and microstructural parameters of CF and CG nanopowders.

Sample	Phase composition (%) RIR method	Hall method		Halder-Wagner method		Lattice parameters (Å)
		Crystallite size (Å)	Microstrain (%)	Crystallite size (Å)	Microstrain (%)	
CF	$CuFe_2O_4$ 100 (2)	32.3 (13)	0.4	16..2 (13)	0	$a = b = 5.8303$ (11) $c = 8.5903$ (13) $\alpha = \beta = \gamma = 90$
CG	$CuFe_2O_4$ 97 (55) CuO 3 (49)	29.4 (12) 2.4	-4 -5	12.5 (41) 15.6 (14)	0 0	$a = b = 5.8417$ (13) $c = 8.6717$ (2) $\alpha = \beta = \gamma = 90$ $a = 5.604$ (188) $b = 4.506$ (86) $c = 6.365$ (106) $\alpha = \gamma = 90$ $\beta = 92$ (5480)

is four times higher than that in the H-W method. This is attributed to the distortions caused in the crystal lattice of CF and CG [54].

Therefore, it is necessary to note that crystallite size depends on the lattice strain which regulates the overall properties of nanoparticles. Due the reduction in the crystallite size of the

nanoparticles, the pressure is developed on the surface of crystallite interfaces which results in stress. The stress developed leads to crystal lattice strain to expand the unit cell [55].

Furthermore, the lattice constants a and c are calculated using the following relationship [56]:

$$\sin 2\theta = \frac{\lambda^2}{4}\left[\frac{h^2 + hk + k^2}{a^2}\right] + \frac{1}{c^2}, \quad (5)$$

where λ is the wavelength of the XRD radiation source, (h, k, l) miller indies of the diffracting plane corresponding to the particular peak, and a and c are the lattice constants. It is evident that the lattice parameters a and c of CG increase with the increase in crystallite size. This is attributed to the less strain impact upon the addition of rGO to the copper ferrite lattice crystal structure that makes better crystal growth of the sample [57]. The procured lattice parameters of CF and CG are given in Table 1.

3.2. Morphological and Compositional Observations. SEM images of CF and CG are presented in Figures 1(b) and 1(c). The microstructural framework in CF shows spherical nanoparticles with varied particle size and with moderate agglomeration. This is due to the magnetic character which causes magnetic dipolar interaction between $CuFe_2O_4$ nanoparticles [58]. To estimate the particle size distribution of the nanoparticles from the SEM images are obtained using ImageJ software [59]. The particle size distribution curve of CF and CG is shown in Figures 1(d) and 1(e). The average particle size distribution of spherical CF nanoparticles is within a narrow range of 110-130 nm with a calculated mean value of 120 nm. This is significantly higher than the values of the crystallite size estimated by XRD analysis thus suggesting each particle is in fact formed my multiple crystallites. The CG SEM image shows that the $CuFe_2O_4$ nanoparticles are homogenously dispersed onto the surface of graphene layers. The presence of $CuFe_2O_4$ particles in CG hinders the accumulation of graphene sheets allowing them to create multiple pores which are evident from Figure 1(c). The average particle size distribution of CG surface is reduced to 100-120 nm, with a mean value of 106 nm which corroborates with XRD analysis. This decrease in particle size is due to the presence of rGO sheets which restrict grain growth and also function as nucleating centers to promote the crystal formation [60, 61]. Thus, CG SEM image signifies that $CuFe_2O_4$ nanoparticles incorporated within reduced graphene oxide layers manifest high porosity and increased surface area and consequently an expected enhanced adsorption activity.

The elemental composition of CF and CG has been determined by EDX analysis. From the EDX spectra displayed in Figures 1(f) and 1(g), the EDX spectrum of CF and CG is demonstrated at 10 keV. The spectra show the presence of Fe, Cu, and O peaks which confirms the formation of $CuFe_2O_4$ in both CF and CG spectra; besides, the Cu : Fe ratio is compatible to the stoichiometry of the synthesis procedure. In addition to the presence of Fe, Cu, and O in the CG EDX spectrum, the presence of C peak reveals the presence of rGO alongside $CuFe_2O_4$. The quantitative data such as the weight percentage (wt%) and atomic percentage (at%) of CF and CG nanocomposite are given in the table inset of Figures 1(f) and 1(g). The assessed atomic percentages of CF and CG nanocomposite are in total agreement with the theoretical values. Moreover, the absence of additional elements confirms the purity of the as prepared samples [62].

3.3. Surface Analysis. The textural properties of CF and CG powders have been examined using Brunauer-Emmett-Teller (BET) analysis. This study gives detailed information on the surface area, pore volume, and diameter of the as prepared powders [63]. From Figure 1(h), the nitrogen adsorption/desorption isotherm expresses type IV BET isotherm according to the IUPAC classification, with the presence of a hysteresis loop. The CF samples present a surface area of $0.66\,m^2 \cdot g^{-1}$ and a pore volume of $1.7\,cm^3 \cdot g^{-1}$; then, both increase significantly with the addition of rGO reaching $5.74\,m^2 \cdot g^{-1}$ and $16.9\,cm^3 \cdot g^{-1}$, respectively. The enhancement of surface area of CG by almost five times compared to CF implies that $CoFe_2O_4$ nanoparticles are well incorporated with regular distribution onto rGO sheets. This favors the production of more reactive sites which will be accompanied by an effective adsorption activity [64, 65].

The (Barrett-Joyner-Halenda) BJH method has been adopted to verify the bimodal mesoporous size distribution in CF and CG powders using the desorption arm in the presented Figure 1(h) [66]. The calculated surface area, pore volume, and diameter of CG are greater in comparison with those of CF (Table 2).

3.4. Magnetic Studies. The magnetic behavior of the as-prepared pure CF and CG powders has been investigated by recording the magnetization *vs.* magnetic field (M-H) curves, as shown in Figure 1(i), and the corresponding magnetic properties are presented in Table 3. It is clearly apparent from the figure that both samples possess soft ferromagnetic behavior, because it possesses near-zero magnetostriction. The saturation magnetization (M_s) for CF $37.11\,emu \cdot g^{-1}$ then slightly decreases for CG ($33.84\,emu \cdot g^{-1}$) upon the addition of rGO. This is attributed to the low spin polarization in $Fe - 3d$ valence states which is related to the high surface area and volume [67, 68]. The presence of nonmagnetic rGO sheets also favors the reduction of M_s value. This was reported also by Hussain et al. [69] that the weak magnetic rGO layer upon addition of nickel decreased the saturation magnetization of Ni-rGO nanocomposite compared to that of bare nickel ferrite. However, the values of coercivity (H_c) and remanence magnetization (Mr) of CG are found to be greater compared to those of CF: 82.66 Oe and $5.42\,emu \cdot g^{-1}$ compared to 14.91 Oe and $0.99\,emu \cdot g^{-1}$, respectively. This increase may correspond to the decrease in the average distance between the microscopic particles in the presence of rGO, which consequently intensify the interaction between interparticle [70, 71].

The remnant ratio (or)/squareness ratio (Mr/Ms) of a magnetic material is an essential parameter which corresponds to its anisotropy. These values represent the

Table 2: BET characteristics of CF and CG nanopowders.

Sample	Average pore diameter (nm)	Average pore volume $(cm^3 \cdot g^{-1}) \times 10^3$	BET $(m^2 \cdot g^{-1})$
CF	6.79	1.7	0.66
CG	11.92	16.9	5.74

indiscriminately oriented single axial particles along the cubic magnetocrystalline anisotropy [72]. It has been examined that the squareness ratio which is significantly above 0.5 depicts that the material is single domain and below 0.5 is ascribed to multiple domain structure where domain wall activity of particles changes its orientation very easily with applied field [73]. In the present study, the estimated squareness ratio value of CF and CG at room temperature is demonstrated in Table 3. It is visible that the reported values of CF (0.05) and CG (0.16) correspond to the multiple domain particles. The values indicate the presence of noncollaborative single domain particles with cubic anisotropy being present in the nanoparticles. The excellent magnetic nature of CG nanocomposite can be used as a magnetic adsorbent for easy separation by an external magnet from any aqueous solution. This characteristic also helps to maintain the adsorbent for reutilization in the adsorption process.

3.5. Barium Adsorption Studies. Further, adsorption experiments of barium ions from the aqueous solution using CF and CG powders have been performed in batch mode, in order to determine the impact of bare ferrite and the rGO-based ferrite nanocomposite on the adsorption efficiency and the involved mechanism. The two important properties of adsorption process such as the contact time and the pH of the solution have been examined. Figure 2(a) indicates that the CF removal efficiency reaches 68% and then increases up to 78% for CG in 120 min. The observed enhancement is due to the significant role of rGO, since it increases the surface area, pore volume, and more available active sites because of its layered nanostructure.

3.5.1. Effect of pH. It is certain that the pH of the solution regulates the barium adsorption performance in aqueous solution [74]. It also governs the active surface charge and the functional group species present at the surface of the adsorbent [1, 2]. This assists the barium ions to not easily form complexes and hydrolyze [4]. In order to determine the effect of pH change on the removal activity and the optimal pH, this set of experiments has been conducted within a pH range 3–11 by using a fixed mass of adsorbent 10 mg in 25 mL barium solution. Figure 2(b) illustrates the impact of pH value on the barium removal activity of both CF and CG. It can be observed that the increase of pH within the range 3–7 enhances the removal efficiency of barium ions followed by a steady decrease with further pH up to 11. This is because at pH 7, it shows the absence of surface charge on the adsorbent whereas at pH lower to 7. Coulomb electrostatic repulsion occurs between the positively charged adsorbents and the negative species of Ba(II) which hinder the removal of Ba(II) ions. Also, the rapid decrease in the removal efficiency with increase in pH in the range 7–11 is due to the progressive deprotonation of the hydroxyl groups on the surface of adsorbent particles which therefore cause repulsion between the Ba(II) ions and the negatively charged adsorbent that tends to inhibit the removal activity [75, 76]. The figure also depicts that pure CF nanoparticles exhibit ~38% removal of Ba(II) ions at pH 7 whereas CG nanocomposite displays much improved adsorption efficiency reaching ~73%. This clearly testifies the effect of rGO on the adsorption activity and the removal potency of Ba(II) ions. Hence, the adsorption activity of the as-prepared $CuFe_2O_4$/rGO nanocomposite depends significantly on the pH. The optimized pH 7 has been used for further experiments.

The point of zero charge (P_{ZC}) of CF and CG is measured to examine the change in the pH environment. The P_{ZC} of CF is 7.2, and that of CG is found to be 6.8 which is displayed in Figure 3. In general, positive charge is developed at $pH < P_{ZC}$ and the generation of negative charge occurs at $pH > P_{ZC}$. At $pH = P_{ZC}$, the charge developed is neutral. From the obtained results, it is significant to note that the surface charge of CF is positively charged at pH lesser than the obtained P_{ZC} value of 7.2, and that of CG is 6.9. In this study, maximum adsorption is achieved for CF and CG at pH 7. Hence, the outcome acquired shows that both the magnetic adsorbents have wide functions in pH conditions, which is beneficial to adsorption of heavy metal studies.

3.5.2. Adsorption Kinetics Study. The kinetics of the adsorption is pivotal as it describes the contact time in the removal of Ba(II) ions, the rate of the solute uptake, and the adsorption capacity of the adsorbent [34]. The adsorption kinetics has been evaluated using pseudo-first-order, pseudo-second-order, and Elovich models, which are expressed below.

The pseudo-first-order reaction is regularly employed for the liquid and solid sorption; the linearized rate determining expression is given by the Equation (6) [43]:

$$\ln (q_e - q_t) = \ln q_e - \frac{k_1}{2.303} t, \tag{6}$$

where k_1 is the pseudo-first-order rate constant (min^{-1}) and q_e and q_t are the adsorbed amounts (mg/g) at equilibrium and at any time t (min).

The pseudo-second-order is considered for the chemical reactions that occur on the surface of the adsorbent; the linearized expression is given in Equation (7) [43]:

$$\frac{t}{q_t} = \left[\frac{1}{k_2 q_e^2}\right] + \frac{1}{q_e} t, \tag{7}$$

where k_2 is the pseudo-second-order rate constant (g/(mg·min)).

The linearized Elovich model is used to analyze the liquid sorption on the surface and pores of the adsorbents; the expression is given in Equation (8) [77]:

$$q_t = \frac{1}{\beta} \ln (\alpha\beta) + \frac{1}{\beta} \ln t, \tag{8}$$

Table 3: Magnetic properties of prepared CF and CG nanopowders.

Sample	Saturation magnetization Ms (emu/g)	Magnetic remanence Mr (emu/g)	Coercivity Hc (Oe)	Squareness ratio (Mr/Ms)
CF	37.11	1.99	14.91	0.05
CG	33.84	5.42	82.86	0.16

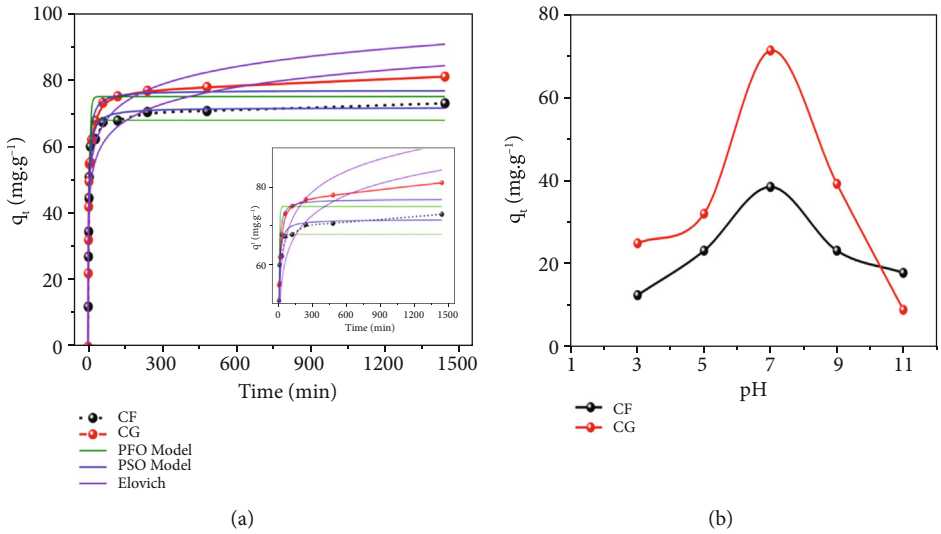

Figure 2: (a) Comparison of equilibrium time models for Ba(II) adsorption on CF and CG nanocomposites and nonlinear plot. (b) Effect of pH value on the equilibrium adsorption capacity of Ba(II) by CF and CG.

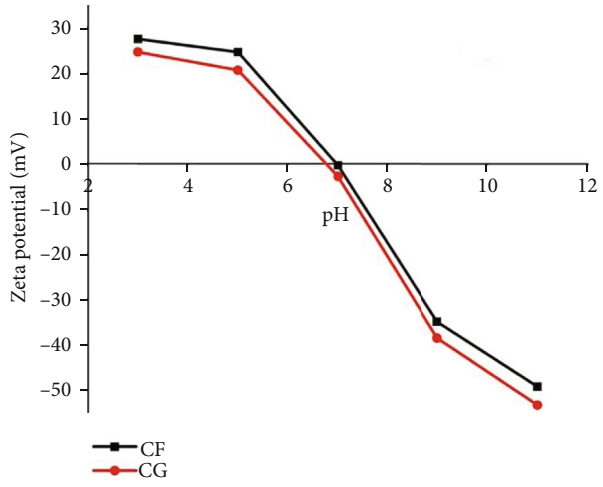

Figure 3: Zero-point charge curve on CF and CG.

where α and β are initial adsorption rate (mg/g·min) and desorption constant (g/mg) corresponding to the Elovich model [78, 79].

The obtained experimental data were fitted with the above-mentioned kinetic models. The plots drawn with $\ln(q_e - q_t)$ vs. t for pseudo-first-order, t/q_t vs. t for pseudo-second-order, and q_t vs. Lnt for Elovich models are presented in Figures 4(a) and 4(c). The parameters k_1 and k_2 acquired from the intercept and q_e (adsorption amount) calculated from the slope of the plots are given in Table 4. The kinetic study results of CF and CG using pseudo-first-order model do not fit accurately; hence, it fails to explain the adsorption kinetics. Hence, the pseudo-second-order kinetics model has been used; the R^2 values are higher with 0.9993 for CF and 0.9994 for CG than the pseudo-first-order kinetics model. Also, the $q_{e(\mathrm{Cal})}$ values of CG are in close agreement with the experimental data. Thus, the suitable pseudo-second-order model explains the rate limiting step in adsorption of Ba(II) ions onto CF and CG nanopowders. This confirms the chemisorption reactions involved which cause valence forces by the electron exchanges between the adsorbent and Ba(II) ions [79]. In addition to this, the Elovich kinetic model was studied to understand the chemical adsorption of Ba(II) ions. However, on considering the R^2 value of the Elovich model, it is found to be inappropriate as the values are not in favor with measuring barium adsorption on CF and CG nanocomposite [80].

Another model has been also tested in order to investigate the possible diffusion mechanism [81], namely, Weber-Morris kinetic model (intraparticle diffusion). The heavy metal adsorption occurs when metal ions present in the bulk solution get diffused into the outer surface of the adsorbent. This mechanism depends on the reactiveness of the surface area and the density of the liquid layer. The feasible intraparticle diffusion rate limiting expression is given by the following equation [34]:

$$q_t = k_{dif} t^{1/2} + C, \tag{9}$$

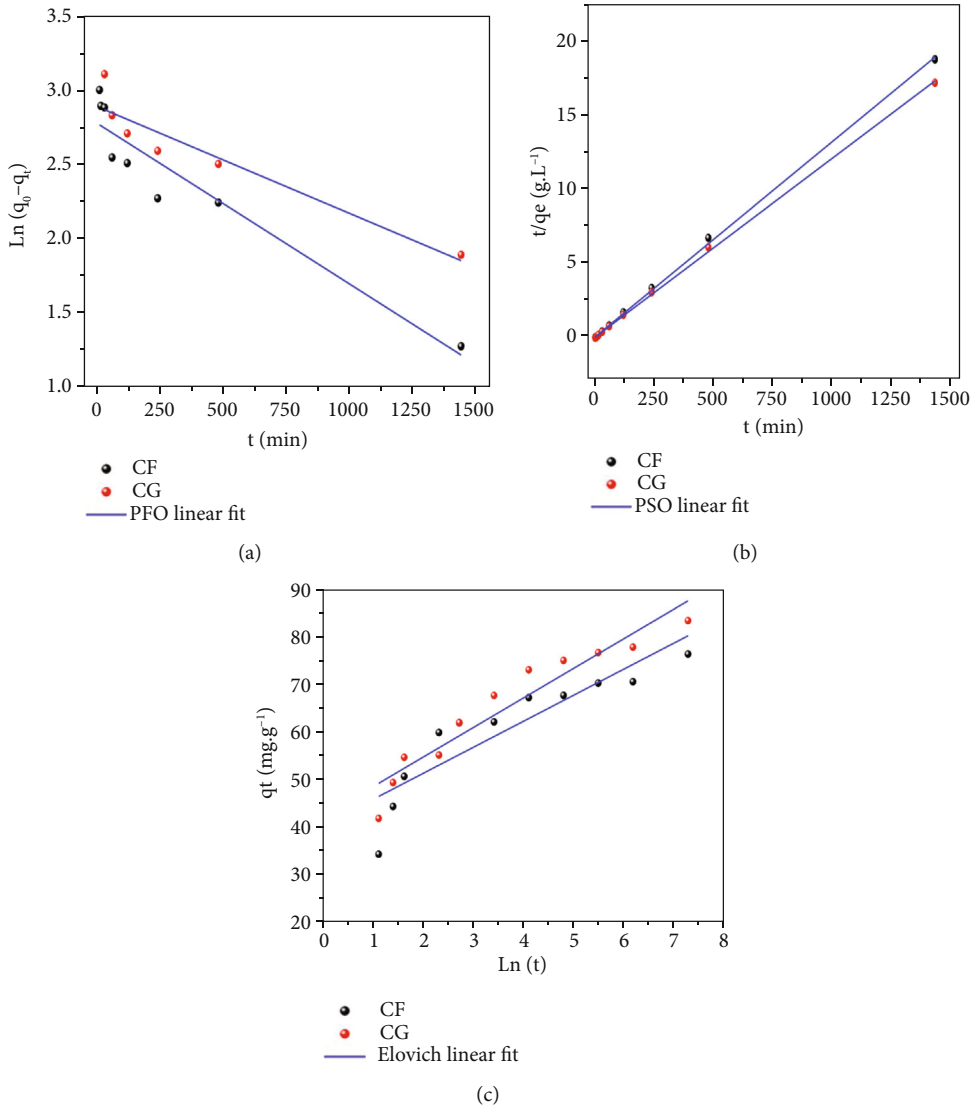

Figure 4: (a) Pseudo-first-order, (b) pseudo-second-order, and (c) Elovich kinetic models for adsorption of Ba(II) for CF and CG nanocomposites.

Table 4: Kinetics model parameters for the adsorption of Ba(II) by CF and CG nanopowders.

	Pseudo-second-order model					
Adsorbent	$q_{e(\mathrm{Exp})}$ [a] (mg·g^{-1})	$t_{1/2}$ (min)	h_0 (mg·g^{-1}·min^{-1})	$q_{e(\mathrm{Cal})}$ [b] (mg·g^{-1})	$K_2 \times 10^3$ (g·mg^{-1}·min^{-1})	r^2
CF	80	6.65	11.47	76.22	1.97	0.9993
CG	85	7.94	10.48	83.26	1.5	0.9994
Pseudo-first-order model					Elovich model	
	$q_{e(\mathrm{Cal})}$ [b] (mg·g^{-1})	$K_1 \times 10^3$ (min^{-1})	r^2	β	$\alpha \times 10^{-4}$	r^2
CF	15.96	10.8	0.9061	0.184	9553.5	0.8041
CG	17.87	7.2	0.9227	0.162	6076.3	0.9161

where k_{dif} is rate constant of intraparticle diffusion (mg/(g·min$^{1/2}$)) which is acquired from the slope of the plot q_t vs. $t^{1/2}$ and C is the intercept obtained in the plot corresponding to the width of the boundary layer. All the calculated parameters are given in Table 5; the R^2 values obtained from intraparticle diffusion model are 0.9856 and 0.9874 for CF and CG,

Table 5: Intraparticle diffusion and mass transfer model parameters for the adsorption of Ba(II) by CF and CG nanopowders.

Adsorbent	Intraparticle diffusion						Mass transfer kinetics		
	K_{1diff} ($mg{\cdot}g^{1}{\cdot}min^{1/2}$)	C_1	R^2	K_{1diff} ($mg{\cdot}g^{1}{\cdot}min^{1/2}$)	C_2	R^2	K_O	D	R^2
CF	31.19	18.48	0.9856	0.88	64.88	0.9707	0.88	64.88	0.9707
CG	27.16	5.43	0.9874	2.69	71.19	0.9851	2.69	71.19	0.9851

respectively, which are higher than the values of the pseudo-first order kinetics model. This is owing to the fact that the outer layer of the adsorbent is in close affinity to Ba(II) ions [38]. Generally, if the straight line of the plot passes through the origin, the chemical adsorption is governed by the intraparticle diffusion kinetics. In this study, Figure 5(a) shows multilinear lines for both CF and CG, which indicates that this model is not the only rate-controlling factor. This suggests that the adsorption of Ba(II) ions is also influenced by the kinetics activity [82]. The first line corresponds to the transfer of Ba(II) ions through the boundary layer into the surface of the adsorbent which is governed by macropore diffusion, whereas the second line shows the slow diffusion process which controls the adsorption of Ba(II) ions, which is controlled by the micropore and mesopore dispersion. The values of C from the intercept render the amount of resistance on the mass transfer which arises from the thickness of the boundary layer [83]. The greater values of$C_2$when compared to those ofC_1reveal that the rate of adsorption is higher in (phase I) C_1. This is because C_1 shows reduced boundary layer thickness in which the adsorption is not controlled by the internal diffusion. Hence, the adsorption of Ba(II) ions onto CF and CG adsorbents partly fits the diffusion kinetics model with agreeable R^2 values. This is in accordance with the reported data [84].

The adsorption kinetics is also controlled by the mass transfer reactions. The kinetic expression of the mass transfer model is expressed by the following equation [38]:

$$Ln(C_0 - C_t) = Ln(D) - k_0 \cdot t, \tag{10}$$

where C_0 and C_t are the initial and final concentrations of the metal ion (mg/L), D is the fitting diameter, k_0 is an adsorption constant (min^{-1}), and t is the contact time (min).

The initial step of the intraparticle diffusion process is the mass transfer reactions, which occurs due to the driving forces that cause the transfer of chemical compounds present in the fluids [85]. The plot from the Figure 5(b) shows that the obtained lines are nonlinear which strongly does not encourage the adsorption of Ba(II) ions using mass transfer reactions. The parameters such as diffusion constant k_0 and the fitting diameter D are given in Table 5. The obtained low values of R^2 suggest that the sorption process does not favor diffusion and mass transfer by convection factors. This is because the movement of ions in the liquid solution is interrupted due to the molecular collisions.

The nonlinear plots of all the kinetic models such as pseudo-first-order, pseudo-second-order, and Elovich are drawn against the time (t) and amount of metal adsorbed q_t ($mg{\cdot}g^{-1}$) at any time. The adsorption of Ba(II) metal ions has been investigated with a much longer stirring time of about 25 h. The equilibrium action of the sorption and the kinetic plots is displayed in Figure 2(a). The plots exhibit that the removal efficiency of the adsorbents increases with the increase in the contact time. It shows that at the initial stage of 120 min, the reaction kinetics is visibly high with an adsorption capacity of 76% for CG and 68% for CF. Nevertheless, upon further increase of the contact time, the adsorption reaction decreases and an equilibrium state is attained. This is probably due to the vacancy that occurred on the surface area of CF and CG adsorbents and their strong affinity to the adsorbate. This leads to a significant drop in reaction with the movement of time and thereby to reach an equilibrium state [78, 79, 86]. As it can be seen in Figure 2(a), the nonlinear plots of the second-order-kinetic models fit better when compared with those of other models. The calculated values of q_e are in accordance with the q_e experimental data with the highest R^2 values.

3.5.3. Adsorption Equilibrium Study. The equilibrium isotherms are used to study the adsorption characteristics such as the correlation between the adsorbent-adsorbate and also the adsorption efficiency of the adsorbent [87].

The equilibrium approach in the current study is designed using four main models, namely, Langmuir, Freundlich, Temkin, and Redlich-Peterson, in order to explain the adsorption of Ba^{2+} ions onto CF and CG magnetic adsorbents. The plots of the isotherms are constructed by the amount of Ba(II) adsorbed at equilibrium (mg/g) to the equilibrium concentration of Ba(II). These isotherms were fitted by means of linear expressions which are expressed below.

The Langmuir isotherm explains the formation of monolayer on the surface of the adsorbents. The adsorbed atoms are situated at definite site with consistent adsorption energy. The linear expression of Langmuir isotherm model is given by Equtaion (11) [45]:

$$\frac{C_e}{q_e} = \frac{1}{q_m K_L} + \frac{C_e}{q_m}, \tag{11}$$

where C_e is concentration of the adsorbate ($mg\,L^{-1}$), q_e is the quantity adsorbed per unit mass of adsorbent ($mg\,g^{-1}$), q_m is the maximum quantity of adsorbate ($mg\,g^{-1}$), and K_L is the Langmuir constant which corresponds to the adsorption quantity ($mg\,L^{-1}$).

This Freundlich isotherm accounts on the heterogeneous surface of the adsorbent which is related to a multilayer adsorption. The linear expression of Freundlich isotherm

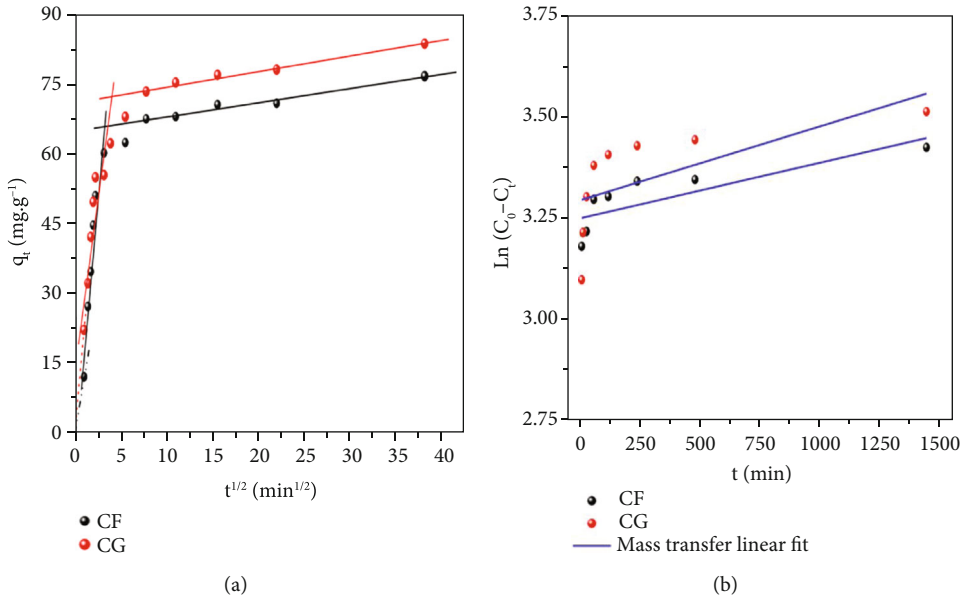

Figure 5: (a) Intra-particle diffusion plots (b) Mass transfer linear fit of CF and CG on the adsorption of Ba(II).

model is given by the following Equation (12) [88]:

$$\ln q_e = \ln K_F + \frac{1}{n} \ln C_e, \tag{12}$$

where q_e is the adsorption capacity at equilibrium (mg·g^{-1}), K_F is the Freundlich constant which corresponds to the quantity adsorbed, $1/n$ is related to the adsorption intensity, and C_e is the concentration of the adsorbate at equilibrium (mg L^{-1}).

The Temkin isotherm is characteristics of the relationship between the adsorbent and the adsorbate. The surface of adsorbent is heterogeneous with the ionization energy evenly distributed. The isotherm also infers that the temperature (heat) of the molecules in the layer during the adsorption process decreases linearly in consequence of the increase in adsorption quantity. The linear expression of Temkin isotherm model is given by Equation (13) [84]:

$$q_e = \frac{RT}{b} \ln K_T + \frac{RT}{b} \ln C_e, \tag{13}$$

where q_e is the adsorption capacity at equilibrium (mg·g^{-1}), b is the Temkin constant in connection to the heat during the adsorption process (J·mol^{-1}), R is the universal gas constant, and K_T is the Temkin isotherm constant (L·g^{-1}).

The Redlich-Peterson isotherm involves the combination of Langmuir and Freundlich isotherms. The model holds linearity in the exponential and numerator function which correspond to the adsorption equilibrium for a different concentration of adsorbate. Due to their flexibility, it can be suitable for homogenous and heterogeneous adsorption systems [88]. The linear expression of Redlich-Peterson isotherm model is given by the Equation (14) [89]:

$$\frac{\ln q_e}{C_e} = \beta \ln C_e - \ln A, \tag{14}$$

where β corresponds to the exponent between 0 and 1 and A is the intercept in the plot of Redlich-Peterson isotherm.

The adsorption isotherm experiments were performed for CF and CG nanopowders. The linear plots ofC_e/q_evs.C_e, ln q_e vs.ln C_e,$q_e$vs.ln C_e, andln $q_e$vs.ln (C_e) correspond to Langmuir, Freundlich, Temkin, and Redlich-Peterson isotherm models are presented in Figures 6(a)–6(d). The acquired parameters from each model are given in Table 6.

Based on the experimental results from Langmuir isotherm model, the correlation coefficient (R^2) values of CF and CG are 0.9926 and 0.9934, which demonstrate that the adsorption of Ba^{2+} ions is better fitted in this model. The primary dimensionless constant R_L values are 0.059 and 0.913, which are lesser than 1 and greater than 0 suggest that the isotherm is favorable. The obtained q_m values are 86.58 and 161.55 mg·g^{-1} while K_L values are 0.0094 and 0.0059 L·mg^{-1}, respectively, for CF and CG. This indicates the occurrence of a homogenous adsorption with constant adsorption energy on the adsorbent surface [43].

The recorded R^2 values of Freundlich isotherm model are 0.9197 and 0.9789, and the n values are greater than 1. The values of the adsorption capacity K_F for CG is higher than CF. Hence, the Freundlich isotherm is favorable and validates the heterogeneity for both CF and CG with minor deviation values [90]. However, the R^2 values are lower in comparison to Langmuir isotherm, and for that reason, the Langmuir model is considered to be more suitable.

From the Temkin isotherm experimental results, the R^2 values are 0.9550 and 0.8405 and the values of b are 177.58 J·mol^{-1} and 122.96 J·mol^{-1} for CF and CG, respectively. The low correlation coefficient values of CG suggest that the model does not fit the Temkin isotherm model when compared to CF. This is due to the weak interaction of Ba^{2+} ions and CG adsorbent [91].

Based on Redlich-Peterson isotherm results, the R^2 values are 0.9766 and 0.9939 for CF and CG, respectively, while the exponent β values lie in the range 0-1. When β

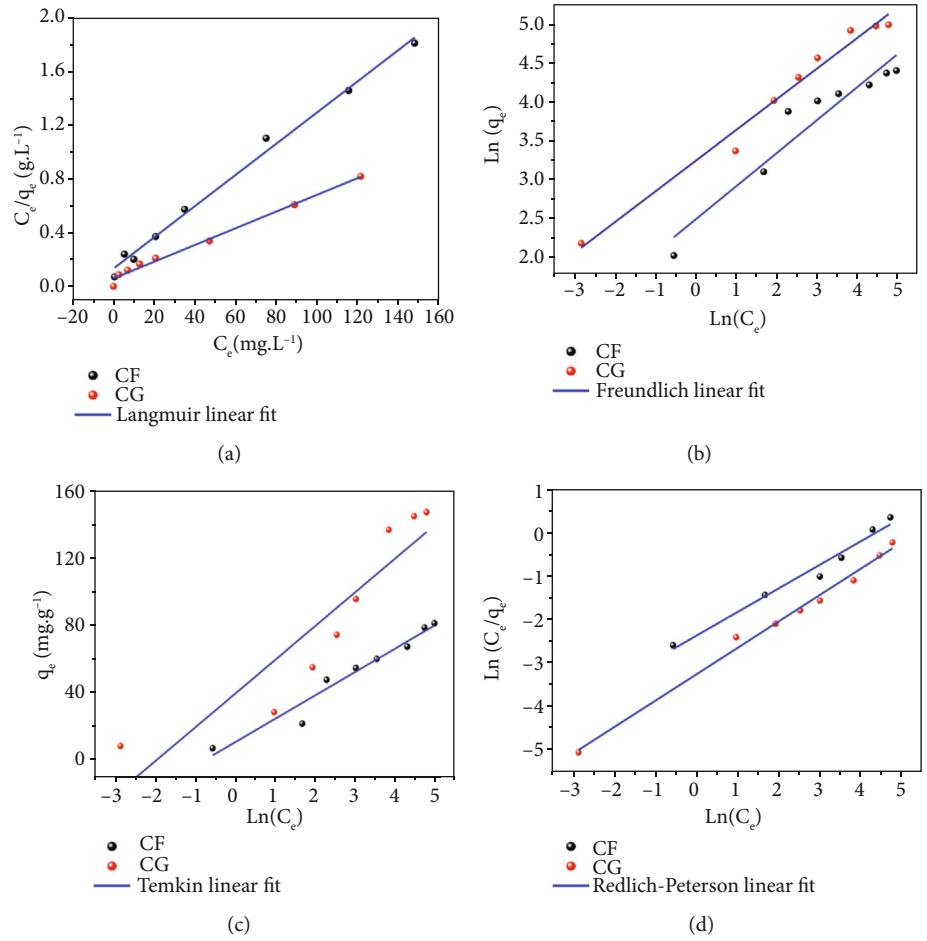

FIGURE 6: Assessment of isotherm models for Ba(II) adsorption on CF and CG nanocomposite by (a) Langmuir, (b) Freundlich, (c) Temkin, and (d) Redlich-Peterson.

TABLE 6: Different model Isotherm constants for the adsorption of Ba(II) by CF and CG nanopowders.

Equilibrium model	Parameters	CF	CG
Langmuir	Q_m (mg·g^{-1})	86.58	161.55
	K_L (L·mg^{-1})	9.4x10^{-4}	5.9x10^{-4}
	R_L (L·mg^{-1})	0.059	0.9132
	R^2	0.9926	0.9934
Freundlich	n	2.35	2.53
	K_F (L·mg^{-1})	11.98	25.55
	R^2	0.9197	0.9789
Temkin	B (J·mol^{-1})	177.58	122.96
	K_T (L·mg^{-1})	2.18	7.15
	R^2	0.9550	0.8405
Redlich-Peterson	β	0.541	0.605
	A (L·g^{-1})	10.51	25.55
	R^2	0.9766	0.9939

= 0, it approaches the Freundlich isotherm that corresponds to high-liquid phase concentration. If $\beta = 1$ (values that are close to 1), it approaches the Langmuir isotherm model because of low liquid-phase concentration. In the current study, the obtained values of β are 0.541 and 0.605 which is significantly greater than 0 that corresponds to the Langmuir equation [88, 89, 92]. This suggests that the values are in accordance with the Langmuir conditions. Also, from Table 6, the maximum adsorption capacity A values in Redlich-Peterson isotherm are 10.51 L·g^{-1} for CF and 25.55 L·g^{-1} for CG.

On the basis of the R^2 values obtained from the different isotherms, the best fitted isotherm is Langmuir. The following is the interpreted isotherm order based on its accuracy, Langmuir > Redlich-Peterson > Freundlich > Temkin isotherm models.

The nonlinear fit for the aforementioned isotherms is shown in Figure 7. By comparing the calculated nonlinear plot with the experimental data, the Langmuir isotherm matches well with the experimental data.

3.6. Thermodynamic Studies. The effect of temperature from 25 to 55 ± 1°C on the adsorption of Ba(II) onto copper ferrite (CF) and copper ferrite/rGO (CG) nanocomposite was

investigated. From the Figure 8, it is found that the adsorption of Ba(II) using CF and CG nanocomposite increases with the increase in temperature. Moreover, high temperature favors the adsorption capacity of CF and CG which is attributed to the increase in diffusion of Ba^{2+} into the pores of the CF and CG adsorbents. The thermodynamic parameters which include Gibbs free energy change (ΔG°), enthalpy change (ΔH°), and entropy change (ΔS°) were estimated from the intercept and slope of the Van't Hoff plot. The thermodynamic mathematical formula is given below [82]:

$$\Delta G^\circ = -RT \ln K^\circ, \tag{15}$$

where R refers to ideal gas constant (8.3145 J mol^{-1} K^{-1}), T is the absolute temperature of the solution (Kelvin), K° is the thermodynamic equilibrium constant which is obtained by plotting ln (C_s/C_e) versus C_s C_s is the quantity of heavy metal adsorbed per unit gram of adsorbent (mmol/g), and C_e is the equilibrium concentration of the heavy metal ions (mmol/mL). ΔH° and ΔS° are obtained by plotting ln Kd versus $1/T$ using the following Vant Hoff equation which is given in Equation (16), and the plot of CF and CG is given in Figures 8(b) and 8(c) [82].

$$\ln K^\circ = \frac{\Delta S}{R} - \frac{\Delta H}{RT}. \tag{16}$$

The values of ΔG°, ΔH°, andΔS° parameters for adsorption of Ba(II) using CF and CG adsorbents are given in Table 7. The obtained negative values of ΔG° at all measured temperature represent the spontaneous reaction. In addition, the negative values of ΔG° increase with the increase in temperature which confirms the feasibility of adsorption reaction at high temperature. The positive value of ΔH° for both CF and CG adsorbent reveals the endothermic reaction of the adsorption process. This is because the well-hydrated metal ions require high energy to break and proceed for adsorption process. Moreover, the adsorption capacity is enhanced at higher temperature due to the increase in pore size and activation of outer surface of adsorbent [83]. For these reasons, high temperature favors the effective adsorption process of heavy metal [84]. The positive value of ΔS° for CF and CG adsorbents corresponds to randomness in adsorbent-adsorbate interaction during the adsorption process. The positive value of ΔS° shows high affinity of heavy metal ions towards CG nanocomposite, which means more assessability and randomness of the deeply found active sites in CG nanocomposite when compared to CF.

3.7. Stability Evaluation of CF and CG Adsorbents. To study the stability of CF and CG adsorbents, water stability, effect of pH, and effect of concentration stability of CF and CG adsorbents were investigated. In addition, the changes in crystal structure of the adsorbents were also studied.

3.7.1. Water Stability of CF and CG. The effect of water stability of CF and CG adsorbents was supervised using XRD analysis. It is visible from the XRD patterns of CF and CG adsorbents are unchanged, which indicate that soaking the

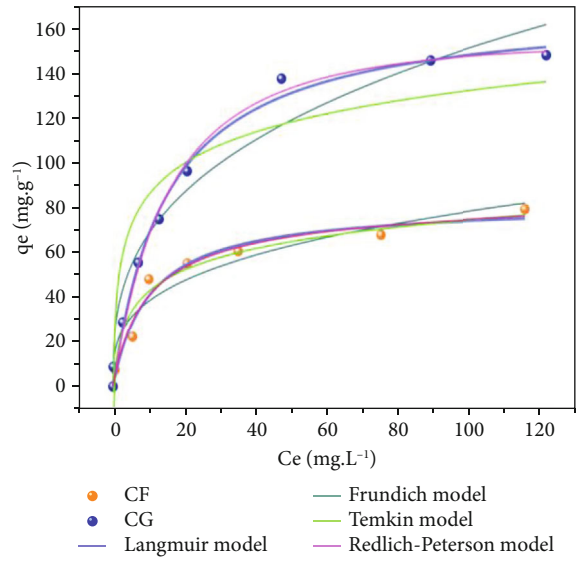

Figure 7: Comparison of isotherm models for Ba(II) adsorption on CF and CG nanocomposites and nonlinear plot.

adsorbents in water for 5 days does not show any variation in the crystal structure of the adsorbent materials. This confirms the water stability of the prepared nanoadsorbents which is shown in Figures 9(a) and 9(b). However, the intensity of the diffraction peaks is slightly lowered at the fifth day which signifies that the CF and CG adsorbents are in the initial stages to dissolve in water [93]. Further, the adsorbents were collected to estimate the adsorption capacity towards Ba(II). The results show no considerable reduction in the adsorption quantity of Ba(II) by the CF and CG adsorbents after exposure to water for 5 days (Figure S1).

3.7.2. Effect of pH on Stability of CF and CG Adsorbents. The effect of pH on the stability of CF and CG adsorbents was investigated in the range 3-11. The XRD results from Figures 9(c) and 9(d) confirm that the adsorbents could be employed for a broad range of pH with no change in crystal structure. The main XRD diffraction peaks of CF and CG are retained; however, some peaks shifted to weak low-intensity peaks. At pH > 1, the diffraction peaks were absent which is because of the dissolved CF and CG adsorbents. At pH < 3, the diffraction peaks show no change in the crystal structure. On the contrary, at pH < 11, the crystal structures are imperfect with broad diffraction peaks corresponding to amorphous form particles [94]. The adsorption of Ba(II) onto CG at pH 7 exhibits 78% as shown in Figure S2. These results manifest that the adsorbents can be used for effective adsorption of Ba(II) ions without preadjusting the pH, as the surface water is around pH 7.

Furthermore, leaching of metal ions is an additional factor that relies on the pH value, and at acidic pH, the solubility of the metal ions increases [95]. The leaching of iron and copper metal ions at different pH for CF and CG adsorbent was examined, and the results are displayed in Figures 10(a) and 10(b). The results reveal that the release of copper metal ions was relatively significant under acidic conditions but

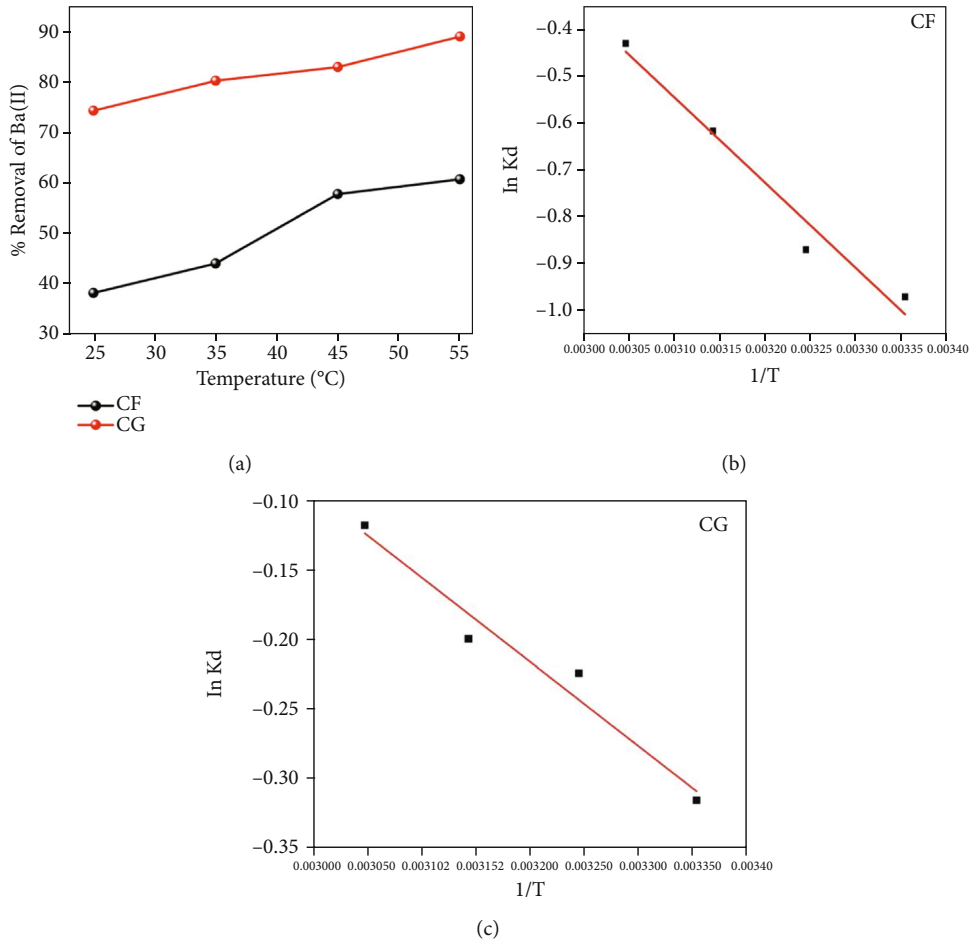

Figure 8: (a) Effect of temperature on the adsorption of Ba(II) onto CF and CG adsorbent; Van't-Hoff plot for adsorption of Ba(II) onto (b) CF and (c) CG.

Table 7: Thermodynamic parameter values for the adsorption of Ba(II) on CF and CG.

Adsorbent	T (K)	ΔG (KJ/mol)	ΔS (J/mol K)	ΔH (KJ/mol)
CF	298	-12.57	42.26	15.08
	308	-12.99		
	318	-13.42		
	328	-13.84		
CG	298	-42.92	14.56	50.38
	308	-44.38		
	318	-45.83		
	328	-47.29		

declined after pH 7, whereas leaching of iron was comparatively low at acidic and basic pH. This signifies that the stability of adsorbents is remarkable under alkaline and neutral medium.

3.7.3. Effect of Ba(II) Concentration on Stability of CF and CG Adsorbent. As shown in Figure S3 (a and b), the crystal structure reveal minor changes in XRD patterns of CG nanocomposite after 45 mg/L Ba(II) concentrations, revealing the stability of the crystal structure after 5 days of water exposure. The leaching of iron and copper after Ba(II) adsorption was also examined on CG nanocomposite with various concentrations. The leaching of copper ions decreased with increasing Ba(II) concentrations from 45 to 65 mg/L, which is shown in Figure S3 (c and d). From Figure 10, the leaching of copper ions was relatively higher, before adsorption of Ba(II), whereas after adsorption, leaching of copper and iron decreased. This is attributed to the coprecipitation between copper and Ba(II) which partially destroys the structure of CG nanocomposite that results from leaching. Hence, leaching of metal ions from CG nanocomposite affects the stability of CG nanocomposite [95].

3.8. Reusability of CF and CG Magnetic Adsorbents. The reusability study of the adsorbents is crucial for economic reasons and for practical applications. The reusability of the adsorbents was examined for 6 repeated cycles under similar operational conditions. After each cycle, the used adsorbents were separated by an external magnet, washed for several times, and dried for reuse for the next cycle [96]. Figure 11 shows the adsorption efficiency of CF and CG on Ba(II) for 6 repeated uses, although the adsorption

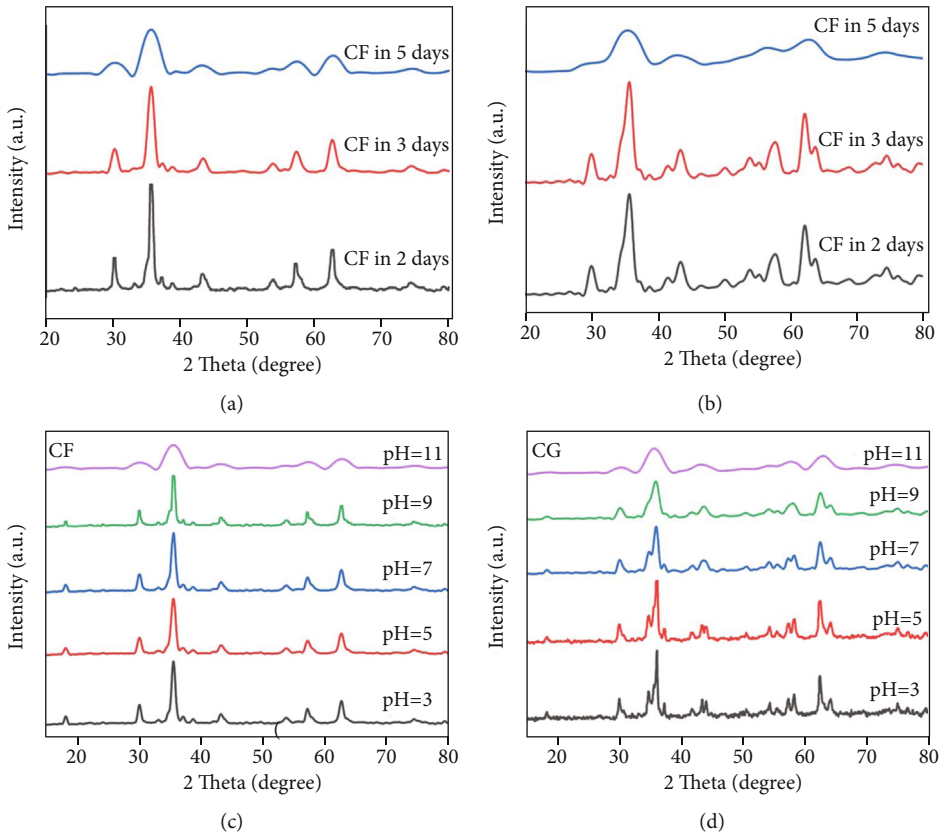

Figure 9: (a) Stability determination using X-ray diffraction patterns of (a) CF and (b) CG exposure in water for five days; (c) CF and (d) CG after soaking in aqueous solution at different pH for 24 h with the adsorbent dosage of 10 mg/L.

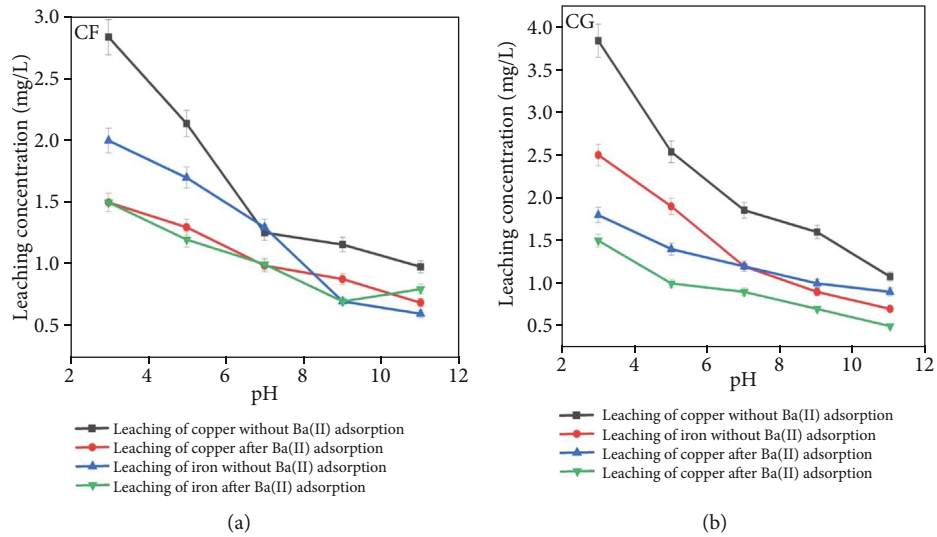

Figure 10: Effect of pH on the leaching of copper and iron on (a) CF and (b) CG.

efficiency of CF and CG was reduced after each cycle the adsorption capacity. However, after 5 cycles, the Ba(II) adsorption capacity using CF adsorbent is 71.23% and that using CG adsorbent is 79.60%. This is due to the partial erosion of the surface of CF and CG adsorbents. Another possible cause is incomplete removal of Ba(II) ions, which gets deposited on the surface of the adsorbents. Hence, the reusability results show that the CF and CG are promising magnetic adsorbents for the removal of barium ions from aqueous solutions and wastewaters.

3.8.1. Adsorption Mechanism. In this study, the obtained results show higher adsorption capacity of CG nanocomposite than CF nanoparticles which can be described by the

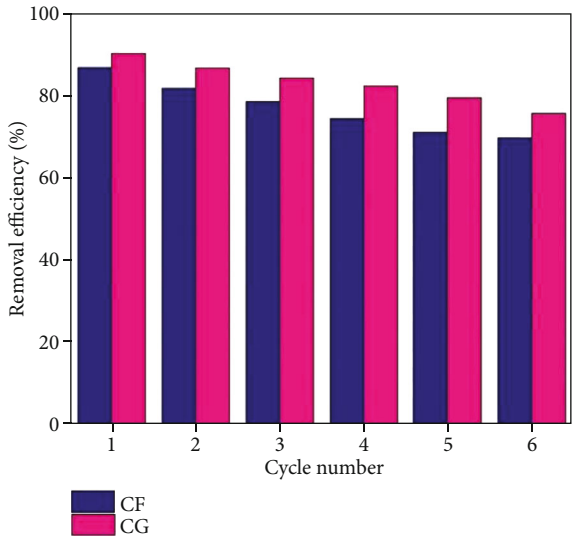

Figure 11: Reusability of CF and CG adsorbents for the removal of Ba(II) through six cycles.

adsorption mechanism involved by the adsorbents and Ba(II) ions. The principal factors such as the pH and the adsorbate-adsorbent interactions are involved during Ba(II) ion removal [97]. On this basis, the adsorption of Ba^{2+} ions follows three main steps [98].

(i) External diffusion: migration of Ba(II) ions from the bulk solution to the adsorbents surface which occurs due to the concentration gradient

(ii) Internal diffusion: migration of Ba(II) ions from the external surface of the adsorbents to the inner pore of the adsorbents

(iii) Attachment of Ba(II) ions to the pore through -COOH and -OH sites

Generally, the physiochemical interactions such as ion exchange, electrostatic interactions, π-π conjugation, and inner sphere surface complexation are responsible for adsorption mechanisms in inorganic material contaminants [98]. The current study is described by the ionic/electrostatic interactions which occur due to the positively charged Ba(II) ions and the negatively charged ions on the surface of CF and CG nanoparticles. Also, the oxygen bearing functional groups such as hydroxyl (-OH) carboxyl (-COOH) and the epoxy groups (C-O) present on the surface of the adsorbents become active sites during the adsorption process. The stated mechanism shows the key role of rGO layer as they contain oxygen bearing functional groups and also involve ionic/electrostatic interactions. Hence, the role of rGO in CG nanocomposite is predominant and shows greater adsorption capacity when compared to CF nanoparticles [64, 98].

The inner sphere surface complexation adsorption mechanism in CF and CG nanocomposite is analyzed using Fourier Transfer-Infrared Resonance (FT-IR) spectroscopy by comparing the recorded spectra of CF and CG loaded with Ba(II) ions with the bare [99], as shown in Figures 12(a) and 12(b). All the spectra show the presence of two main absorption bands around 600 and 400 cm^{-1} that are attributed to Cu-O and Fe-O occupancy sites [65]. The peak at 589 cm^{-1}corresponds to the stretching vibration of Fe^{3+}-O^{2-} in the tetrahedral complexes, and the peak at 482 cm^{-1} is assigned to the stretching vibration of Cu^{2+}-O^{2-} in the octahedral complexes [100]. It is apparent that there exists a shift in peaks' position after adsorption. This variation in the loaded FT-IR spectrum shows potential involvement of other functional groups on the exterior of the adsorbent [101]. The absorption peaks of -C-O, -C-H, Cu-O, and Fe-O are shifted to a lower frequency in Ba(II) loaded CF adsorbent. Fe-O shows significant shift of 589-570 cm^{-1}, and -C-O shows significant shift of 482-417 cm^{-1} in CF adsorbent [102]. This shift in the peaks' position is attributed to the transformation of hydroxyl groups on barium oxide or in the re-formation of C-O stretching vibration in the -COOH during the inner sphere hydroxyl group complexation of Ba(II) ions [96]. The loaded CG nanocomposite also shows the presence of similar band shift which indicates the potential chemical interactions between Ba(II) ions and the functional groups on the surface of CG nanocomposite. However, the bands show slight decrease in the intensity which is due to the electron delocalization on the adsorbent surface when Ba(II) ions are adsorbed. These interactions intensify the effective removal of heavy metal ions [97, 103].

The possible adsorption mechanism of Ba(II) ions on the CG surface using FT-IR analysis is as follows:

$$\begin{aligned}
\mathrm{CG-OH} + \mathrm{Ba^{2+}} &\longrightarrow \mathrm{CG-O^{-}-Ba^{2+}} + 2\mathrm{H^{+}} \\
\mathrm{CG-COOH} + \mathrm{Ba^{2+}} &\longrightarrow \mathrm{CG-COO^{-}-Ba^{2+}} + \mathrm{H^{+}} \\
(\mathrm{CG-OH})_2 + \mathrm{Ba^{2+}} &\longrightarrow (\mathrm{CG-O^{-}})_2 - \mathrm{Ba^{2+}} + 2\mathrm{H^{+}} \\
(\mathrm{CG-COOH})_2 + \mathrm{Ba^{2+}} &\longrightarrow (\mathrm{CG-COO^{-}})_2 - \mathrm{Ba^{2+}} + \mathrm{H^{+}}
\end{aligned} \tag{17}$$

On the basis of the aforementioned reactions, the adsorption mechanism of Ba(II) is achieved by the inner sphere chemical complexations and the electrostatic interactions on the surface of the adsorbent. Banerjee et al. [104] reported the prominent role of pH in the adsorption process, as it determines the surface charge of the adsorbent. Hence, the influence of pH intensified the adsorption capacity as at higher pH, the interaction between the deprotonated hydroxyl groups and Ba(II) ions is high, and ,also the cationic exchanges with the -COOH group also increase [102]. The presence of rGO in CG nanocomposite enabled high selective adsorption sites for an effective removal of Ba(II) ions from the aqueous solution.

3.9. Comparison with Previous Literatures. It is important to achieve maximum adsorption efficiency with the synthesized adsorbents. A comparative study on the previously reported results on the removal of Ba(II) with the obtained results may help to understand the efficiency of the prepared samples (see Table 8). Fard et al. [3] employed the adsorption

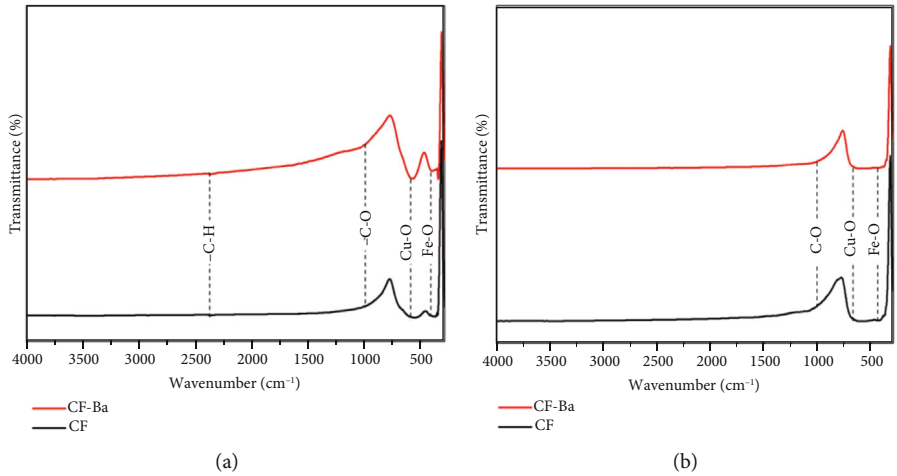

FIGURE 12: FTIR spectra of (a) CF and (b) CG before and after adsorption of Ba(II).

process with the synthesized MXene. The unique properties of MXene showed an adsorption capacity of 9.3 mg/g with the removal efficiency of 100% at pH 6 after 120 min. Majidnia et al. [4] fabricated PVA-alginate beds embedded with TiO_2 and γ-Fe_2O_3 for the effective removal of Ba(II) ions from radioactive wastewater. The nanocomposite showed an adsorption capacity of 19.37 mg/g with 99% of Ba(II) removal at pH 8 in much longer contact time of 150 min. Ghaemi et al. [24] stated that using low-cost dolomite adsorbent, a maximum Ba(II) adsorption capacity of 3.958 mg/g in 120 min at pH 5.5 was attained. Kaveeshwar et al. [25] reported an adsorption capacity of 8.8 mg/g at pH 6 with a very long contact time of 6 h in the adsorption process of Ba(II) using pecan shell-infused activated carbon. Torab-Mostaedi et al. [26] described the removal of Ba(II) using perlite from aqueous solution and showed an adsorption capacity of 2.486 mg/g in 90 min at pH 6.

However, in the present study, CF exhibits an adsorption capacity of 86.6 $mg{\cdot}g^{-1}$ which is almost doubled to reach 161.6 $mg{\cdot}g^{-1}$ for CG in 120 min and at pH 7. This significant enhancement in the adsorption capacity of CG, compared to the removal of Ba(II) by different materials in the literature, is attributed to the incorporation of $CuFe_2O_4$ nanoparticles on the graphene sheet layers. The CG nanocomposite containing oxygen functional group increases the number of vacancy sites. Thereby, both factors favor the adsorption capacity on the removal of Ba(II) ions.

3.9.1. Advantages and Disadvantages of CF and CG Adsorbents. In the current study, CF and CG adsorbents were synthesized as adsorbents for the effective removal of Ba(II). These magnetic nanoadsorbents can be retrieved from aqueous solutions and can be reutilized for up to five cycles by following easy washing and centrifugation or filtration methods. Among both the adsorbents, CG attract their attention due to its structure, high surface area, magnetic property, and stability. However, after five cycles, the efficiency of the adsorbents decreases which is due to the changes that occur on the surface of adsorbents. Moreover, the adsorption performance of CG adsorbent was comparable and acceptable when compared to other reported nanocomposite materials (see Table 8). Hence, CG adsorbent can be extremely used for potential application in heavy metal removal from wastewater.

4. Conclusion

Concisely, $CuFe_2O_4$ (CF) and $CuFe_2O_4$/rGO (CG) magnetic nanopowders were synthesized through a simple and eco-friendly method by using a commercially available microwave. Structure, morphology, and surface studies indicated the formation of spherical spinel ferrite with a surface area of 0.66 m^2g^{-1} and 5.74 m^2g^{-1} for CF and CG. The removal tests of Ba(II) ions from aqueous solution manifested promising and distinctive capability of both CF and CG. Furthermore, the pH-dependent adsorption analysis indicated that the adsorption process obeyed pseudo-second-order rate kinetics. The well-fitted Langmuir model demonstrated an excellent adsorption capacity of 86.6 $mg{\cdot}g^{-1}$ for CF and 161.6 $mg{\cdot}g^{-1}$ for CG adsorbents, achieved under the optimized parameters of 10 mg of adsorbent dose in 25 mL solution at pH 7. A thermodynamic study reveals that the reaction is endothermic and spontaneous. The CG adsorbent exhibited strong chemical and water stability, which could be utilized for removing Ba(II) under various concentrations and wide pH range. In addition, the effect of rGO on the adsorption mechanism of Ba(II) was also studied in detail, hence underlying the principal role of rGO. The rich adsorption sites onto rGO layer enable enhanced adsorption activity of CG nanocomposite when compared to bare CF nanoparticles. Both CF and CG demonstrated soft ferromagnetic behavior with considerable saturation magnetization and hence can be easily separated and reused for several adsorption cycles. To the extent of our knowledge, this is the first report on the adsorption of Ba(II) using copper ferrite and copper ferrite/rGO nanocomposite. This research work suggests the utilization of magnetic CG nanocomposite as effective adsorbent, with high structural stability and excellent adsorption capacity for heavy metal remediation in wastewater.

Table 8: Comparative study of the present work with literature.

Material	Synthesis method and precursors	Phase purity	Particle morphology/ size	Physicochemical properties	Adsorption performance	Reference
$CuFe_2O_4$ $CuFe_2O_4$/rGO	Microwave method 2 g $Cu(NO_3)_2$ + 4 g $Fe(NO_3)_2$ + 2 g lysine 70 mg GO prepared by Hummer's method + 1 : 2 molar $Cu(NO_3)_2$ + $Fe(NO_3)_2$ + 2 g lysine	Pure cubic spinel Composite	Spherical-like (32 nm) Spherical-like (30 nm)	Ms ($CuFe_2O_4$) = 37.11 emu/g SA ($CuFe_2O_4$) = 0.66 $m^2\ g^{-1}$ PV ($CuFe_2O_4$) = 1.7 $cm^3\ g^{-1}$ Ms ($CuFe_2O_4$/rGO) = 33.84 emu/g SA ($CuFe_2O_4$/rGO) = 5.74 $m^2\ g^{-1}$ PV ($CuFe_2O_4$/rGO) = 16.9 $cm^3\ g^{-1}$	Capacity ($CuFe_2O_4$) = 87 $mg \cdot g^{-1}$ Time = 120 min Kinetics = pseudo-second-order Langmuir model (monolayer) Redlich-Peterson model m = 10 mg in 25 mL Ba(II) solution ; pH = 7 ; T = 25°C Capacity ($CuFe_2O_4$/rGO) = 162 $mg \cdot g^{-1}$ Time = 120 min Kinetics = pseudo-second-order Langmuir model (monolayer) Redlich-Peterson model m = 10 mg in 25 mL Ba(II) solution ; pH = 7 ; T = 25°C	This work This work
MXene	Ball mill process 1 : 1 molar ratio of Ti_2AlC + TiC + 50 wt%of HF	Composite	Book-like layer morphology (25 μm)	SA = 13 $m^2\ g^{-1}$	Capacity = 9.3 $mg \cdot g^{-1}$ Time = 120 min Kinetics = pseudo-second-order Langmuir model (monolayer) m = 100 mg MXene in 20 mL barium solution ; pH = 6, T = 25°C	[3]
Maghemite and titania PVA-alginate beads	Co-precipitation method: 2 mL titanium isopropoxide + 2 mL acetyl acetone + 0.5 g urea + 12 g PVA + 1 g alginate + 0.1 g of γ-Fe_2O_3 + 2%$CaCl_2$ + 6%boric acid	Composite	Spherical morphology (15 nm)	−SA = 10.11 $m^2\ g^{-1}$	Capacity = 19.37 $mg \cdot g^{-1}$ Time = 150 min Kinetics = pseudo-second-order Langmuir model (monolayer) m = 10 g maghemite and titania PVA-alginate beads in 200 mL barium solution ; pH = 8 ; T = 25°C	[4]
Dolomite powder	Commercially purchased	Compound	—	SA = 4.76 $m^2\ g^{-1}$	Capacity Sr (II) = 1.172 $mg \cdot g^{-1}$ Capacity Ba(II) = 3.958 $mg \cdot g^{-1}$ Time = 120 min Kinetics = pseudo-second-order Langmuir model (monolayer) m = 1 g of dolomite in 100 mL each of Ba^{2+} and Sr^{2+} solution ; pH = 5.5 ; T = 20°C	[24]
Pecan shell-based activated carbon	Thermal decomposition method Grounded pecan shell + KOH + H_3PO_4 + H_2SO_4 (25 : 1 : 1 molar)	Composite	Flake like morphology (1 μm)	SA = 1517 $m^2\ g^{-1}$	Capacity Sr (II) = 8.8 $mg \cdot g^{-1}$ Capacity Ba(II) = 3.3 mg/g Time = 6 h Kinetics = pseudo-second-order Langmuir model (monolayer) m = 3 g of PSBAC in 50 ml Ba(II)&55 mL Sr (II) solution ; pH = 6 ; T = 30°C.	[25]
Expanded perlite	Commercially purchased	Compound	—	SA = 1.89 $m^2\ g^{-1}$	Capacity Sr (II) = 1.14 $mg \cdot g^{-1}$ Capacity Ba(II) = 2.486 $mg \cdot g^{-1}$ Time = 90 min Kinetics = pseudo-second-order Langmuir model (monolayer) m = 10 mg of expanded pearlite in 18 g/L Sr (II) and Ba(II) solution ; pH = 6 ; T = 20°C	[26]

Data Availability

No data were used to support this study

Ethical Approval

The authors have agreement with all the copyright rules and ethics in publishing that could have appeared to influence the work reported in this paper.

Conflicts of Interest

The authors have no conflict of interest to declare that are relevant to the content of the article.

Acknowledgments

The authors would like to acknowledge Loyola College Management, affiliated to the University of Madras for presuming the necessary organizational facilities to carry out this research work and IIT Madras, University of Bahrain, and Al Imam Mohammad Ibn Saud Islamic University (IMSIU), Saudi Arabia, for providing the characterization facilities.

Supplementary Materials

Figure S1: the adsorption capacities of CF and CG after exposure in water for 5 days with the optimized parameters (initial Ba(II) concentration = 45 mg/L, adsorbent dosage = 10 mg/L, pH = 7, temperature = 28°C). Figure S2: adsorption capacities of CF and CG after soaking in aqueous solutions at different pH for 24 h (initial Ba(II) concentration = 45 mg/L, adsorbent dosage = 10 mg/L, temperature = 28°C). Figure S3: stability determination using X-ray diffraction patterns of (a) CF and (b) CG after treating with different concentrations of Ba(II) (initial Ba(II) concentration from 45 mg/L to 65 mg/L, adsorbent dosage = 10 mg/L, temperature = 28°C, pH = 7); leaching of (c) copper in CF and CG and (d) leaching of iron in CF and CG. *(Supplementary Materials)*

References

[1] B. Abdulkhair, M. Salih, A. Modwi et al., "Adsorption behavior of barium ions onto ZnO surfaces: experiments associated with DFT calculations," *Journal of Molecular Structure*, vol. 1223, article 128991, 2021.

[2] K. B. Fontana, E. S. Chaves, V. S. Kosera, and G. G. Lenzi, "Barium removal by photocatalytic process: an alternative for water treatment," *Journal of water process engineering*, vol. 22, pp. 163–171, 2018.

[3] A. K. Fard, G. Mckay, R. Chamoun, T. Rhadfi, H. P. Homme, and M. A. Atieh, "Barium removal from synthetic natural and produced water using MXene as two dimensional (2-D) nanosheet adsorbent," *Chemical Engineering Journal*, vol. 317, pp. 331–342, 2017.

[4] Z. Majidnia, A. Idris, M. Majid, R. Zin, and M. Ponraj, "Efficiency of barium removal from radioactive waste water using the combination of maghemite and titania nanoparticles in PVA and alginate beads," *Applied Radiation and Isotopes*, vol. 105, pp. 105–113, 2015.

[5] E. M. Fenu, J. O. Brower, and T. E. O'Neill, "Suicide by an unusual compound," *The American Journal of Forensic Medicine and Pathology*, vol. 42, no. 3, pp. 286–288, 2021.

[6] S. Krishna, A. Jaiswal, G. M. Sujata, D. K. Sharma, and Z. Ali, "Barium poisoning with analytical aspects and its management," *International Journal of Advanced Research in Medicinal Chemistry*, vol. 2, no. 1, pp. 20–27, 2020.

[7] M. Peana, S. Medici, M. Dadar et al., "Environmental barium: potential exposure and health-hazards," *Archives of Toxicology*, vol. 95, no. 8, pp. 2605–2612, 2021.

[8] N. C. Fontão, F. V. Hackbarth, D. A. Mayer et al., "A step forward on mathematical modeling of barium removal from aqueous solutions using seaweeds as natural cation exchangers: batch and fixed-bed systems," *Chemical Engineering Journal*, vol. 401, article 126019, 2020.

[9] E. Bazrafshan, L. Mohammadi, A. Ansari- Moghaddam, and A. H. Mahvi, "Heavy metals removal from aqueous environments by electrocoagulation process-a systematic review," *Journal of environmental health science and engineering*, vol. 13, no. 1, p. 74, 2015.

[10] K. C. Khulbe and T. Matsuura, "Removal of heavy metals and pollutants by membrane adsorption techniques," *Applied Water Science*, vol. 8, no. 1, p. 19, 2018.

[11] M. Černá, "Use of solvent extraction for the removal of heavy metals from liquid wastes," *Environmental Monitoring and Assessment*, vol. 34, no. 2, pp. 151–162, 1995.

[12] A. Mudhoo, V. K. Garg, and S. Wang, "Removal of heavy metals by biosorption," *Environmental Chemistry Letters*, vol. 10, no. 2, pp. 109–117, 2012.

[13] M. C. Benalia, L. Youcef, M. G. Bouaziz, S. Achour, and H. Menasra, "Removal of heavy metal from industrial wastewater by chemical precipitation: mechanisms and sludge characterization," *Arabian Journal for Science and Engineering*, vol. 47, no. 5, pp. 5587–5599, 2022.

[14] A. Bashir, L. A. Malik, S. Ahad et al., "Removal of heavy metal ions from aqueous system by ion-exchange and biosorption methods," *Environmental Chemistry Letters*, vol. 17, no. 2, pp. 729–754, 2019.

[15] M. Cataldo Hernández, L. Barletta, M. B. Dogliotti, N. Russo, D. Fino, and P. Spinelli, "Heavy metal removal by means of electrocoagulation using aluminum electrodes for drinking water purification," *Journal of Applied Electrochemistry*, vol. 42, no. 9, pp. 809–817, 2012.

[16] E. G. Abdel-Aziz, M. A. El-Naggar, S. A. Nosier, A. A. Mubarak, M. H. Abdel-Aziz, and G. H. Sedahmed, "Recovery of copper from industrial waste solutions by cementation using a rotating fixed bed of stacked steel screens," *Milling, Metallurgy & Exploration*, vol. 37, no. 2, pp. 453–458, 2020.

[17] S. Singh, D. Kapoor, S. Khasnabis, J. Singh, and P. C. Ramamurthy, "Mechanism and kinetics of adsorption and removal of heavy metals from wastewater using nanomaterials," *Environmental Chemistry Letters*, vol. 19, no. 3, pp. 2351–2381, 2021.

[18] N. M. Mahmoodi, U. Sadeghi, A. Maleki, B. Hayati, and F. Najafi, "Synthesis of cationic polymeric adsorbent and dye removal isotherm, kinetic and thermodynamic," *Journal of Industrial and Engineering Chemistry*, vol. 20, no. 5, pp. 2745–2753, 2014.

[19] U. F. C. Sayago, Y. P. Castro, L. R. C. Rivera, and A. G. Mariaca, "Estimation of equilibrium times and maximum

capacity of adsorption of heavy metals by *E. crassipes* (review)," *Environmental Monitoring and Assessment*, vol. 192, no. 2, p. 141, 2020.

[20] N. M. Mahmoodi, B. Hayati, H. Bahrami, and M. Arami, "Dye adsorption and desorption properties of Mentha pulegium in single and binary systems," *Journal of Applied Polymer Science*, vol. 122, no. 3, pp. 1489–1499, 2011.

[21] N. M. Mahmoodi, F. Najafi, and A. Neshat, "Poly (amidoamine-co-acrylic acid) copolymer: synthesis, characterization and dye removal ability," *Industrial Crops and Products*, vol. 42, pp. 119–125, 2013.

[22] B. Hayati and N. M. Mahmoodi, "Modification of activated carbon by the alkaline treatment to remove the dyes from wastewater: mechanism, isotherm and kinetic," *Desalination and Water Treatment*, vol. 47, no. 1-3, pp. 322–333, 2012.

[23] N. M. Mahmoodi, "Photocatalytic degradation of dyes using carbon nanotube and titania nanoparticle," *Water, Air, and Soil Pollution*, vol. 224, no. 7, p. 1612, 2013.

[24] A. Ghaemi, M. Torab-Mostaedi, and M. Ghannadi-Maragheh, "Characterizations of strontium(II) and barium(II) adsorption from aqueous solutions using dolomite powder," *Journal of Hazardous Materials*, vol. 190, no. 1-3, pp. 916–921, 2011.

[25] A. R. Kaveeshwar, P. S. Kumar, E. D. Revellame, D. D. Gang, M. E. Zappi, and R. Subramaniam, "Adsorption properties and mechanism of barium (II) and strontium (II) removal from fracking wastewater using pecan shell based activated carbon," *Journal of Cleaner Production*, vol. 193, pp. 1–13, 2018.

[26] M. Torab-Mostaedi, A. Ghaemi, H. Ghassabzadeh, and M. Ghannadi- Maragheh, "Removal of strontium and barium from aqueous solutions by adsorption onto expanded perlite," *Canadian Journal of Chemical Engineering*, vol. 89, no. 5, pp. 1247–1254, 2011.

[27] N. M. Mahmoodi, M. Oveisi, M. Bakhtiari et al., "Environmentally friendly ultrasound-assisted synthesis of magnetic zeolitic imidazolate framework - graphene oxide nanocomposites and pollutant removal from water," *Journal of Molecular Liquids*, vol. 282, pp. 115–130, 2019.

[28] N. B. Singh and R. Km, "Copper ferrite-polyaniline nanocomposite and its application for Cr(VI) ion removal from aqueous solution," *Environmental nanotechnology, monitoring & management*, vol. 14, article 100301, 2020.

[29] N. M. Mahmoodi, "Synthesis of magnetic carbon nanotube and photocatalytic dye degradation ability," *Environmental Monitoring and Assessment*, vol. 186, no. 9, pp. 5595–5604, 2014.

[30] Z. Li, Z. Zhao, J. Fan, W. Wang, L. Li, and J. Liu, "Spinel ferrite-enhanced Cr(VI) removal performance of microscale zero-valent aluminum: synergistic effects of oxide film destruction and lattice spacing expansion," *Separation and Purification Technology*, vol. 294, article 121110, 2022.

[31] R. Jayalakshmi, J. Jeyanthi, and K. R. A. Sidhaarth, "Versatile application of cobalt ferrite nanoparticles for the removal of heavy metals and dyes from aqueous solution," *Environmental Nanotechnology, Monitoring & Management*, vol. 17, article 100659, 2022.

[32] W. A. Khoso, N. Haleem, M. A. Baig, and Y. Jamal, "Synthesis, characterization and heavy metal removal efficiency of nickel ferrite nanoparticles (NFN's)," *Scientific Reports*, vol. 11, no. 1, p. 3790, 2021.

[33] B. R. Vergis, R. Hari Krishna, N. Kottam, B. M. Nagabhushana, R. Sharath, and B. Darukaprasad, "Removal of malachite green from aqueous solution by magnetic $CuFe_2O_4$ nanoadsorbent synthesized by one pot solution combustion method," *Journal of Nanostructure in Chemistry*, vol. 8, no. 1, pp. 1–12, 2018.

[34] C. V. Tran, D. V. Quang, H. P. N. Thi, T. N. Truong, and D. D. La, "Effective removal of Pb(II) from aqueous media by a new design of Cu- Mg binary ferrite," *ACS Omega*, vol. 5, no. 13, pp. 7298–7306, 2020.

[35] Y. J. Tu, C. F. You, C. K. Chang, S. L. Wang, and T. S. Chan, "Arsenate adsorption from water using a novel fabricated copper ferrite," *Chemical Engineering Journal*, vol. 198-199, pp. 440–448, 2012.

[36] N. M. Mahmoodi and M. H. Saffar-Dastgerdi, "Clean Laccase immobilized nanobiocatalysts (graphene oxide-zeolite nanocomposites): from production to detailed biocatalytic degradation of organic pollutant," *Applied Catalysis B: Environmental*, vol. 268, article 118443, 2020.

[37] M. Oveisi, M. A. Asli, and N. M. Mahmoodi, "Carbon nanotube based metal-organic framework nanocomposites: synthesis and their photocatalytic activity for decolorization of colored wastewater," *Inorganica Chimica Acta*, vol. 487, pp. 169–176, 2019.

[38] M. Verma, A. Kumar, K. P. Singh et al., "Graphene oxide-manganese ferrite (GO- $MnFe_2O_4$) nanocomposite: one-pot hydrothermal synthesis and its use for adsorptive removal of Pb^{2+} ions from aqueous medium," *Journal of Molecular Liquids*, vol. 315, article 113769, 2020.

[39] N. M. Mahmoodi, F. Moghimi, M. Arami, and F. Mazaheri, "Silk degumming using microwave irradiation as an environmentally friendly surface modification method," *Fibers and Polymers*, vol. 11, no. 2, pp. 234–240, 2010.

[40] H. Astaraki, S. M. Masoudpanah, and S. Alamolhoda, "Effects of fuel contents on physicochemical properties and photocatalytic activity of $CuFe_2O_4$/reduced graphene oxide (RGO) nanocomposites synthesized by solution combustion method," *Journal of Materials Research and Technology*, vol. 9, no. 6, pp. 13402–13410, 2020.

[41] J. C. Fariñas, R. Moreno, A. Pérez et al., "Microwave- assisted solution synthesis, microwave sintering and magnetic properties of cobalt ferrite," *Journal of the European Ceramic Society*, vol. 38, no. 5, pp. 2360–2368, 2017.

[42] A. Shanmugavani, R. Kalai Selvan, S. Layek, and C. Sanjeeviraja, "Size dependent electrical and magnetic properties of $ZnFe_2O_4$ nanoparticles synthesized by the combustion method: comparison between aspartic acid and glycine as fuels," *Journal of Magnetism and Magnetic Materials*, vol. 354, pp. 363–371, 2014.

[43] Y. Zhang, L. Yan, W. Xu et al., "Adsorption of Pb(II) and Hg(II) from aqueous solution using magnetic $CoFe_2O_4$-reduced graphene oxide," *Journal of Molecular Liquids*, vol. 191, pp. 177–182, 2014.

[44] W. S. Hummers and R. E. Offerman, "Preparation of graphitic oxide," *Journal of the American Chemical Society*, vol. 80, pp. 311–336, 1958.

[45] X. Y. Tu and K. Y. Shu, "X-ray diffraction study on phase transition of orthorhombic $LiMnO_2$ in electrochemical conversions," *Journal of Solid State Electrochemistry*, vol. 12, no. 3, pp. 245–249, 2008.

[46] L. Kumar, P. Kumar, A. Narayan, and M. Kar, "Rietveld analysis of XRD patterns of different sizes of nanocrystalline

cobalt ferrite," *International Nano Letters*, vol. 3, no. 1, p. 8, 2013.

[47] W. Zhang, B. Quan, C. Lee et al., "One-step facile solvothermal synthesis of copper ferrite-graphene composite as a high-performance supercapacitor material," *ACS Applied Materials & Interfaces*, vol. 7, no. 4, pp. 2404–2414, 2015.

[48] P. Raji and K. B. Kumar, "Structural, elastic and magnetic properties of Ca doped copper ferrite nanoparticles," *Physica B: Condensed Matter*, vol. 632, article 413759, 2022.

[49] R. Dhanda and M. Kidwai, "Magnetically separable $CuFe_2O_4$/reduced graphene oxide nanocomposites: as a highly active catalyst for solvent free oxidative coupling of amines to imines," *RSC Advances*, vol. 6, no. 58, pp. 53430–53437, 2016.

[50] D. Nath, F. Singh, and R. Das, "X-ray diffraction analysis by Williamson-Hall, Halder-Wagner and size-strain plot methods of CdSe nanoparticles- a comparative study," *Materials Chemistry and Physics*, vol. 239, article 122021, 2020.

[51] M. S. Abd El-Sadek, H. S. Wasly, and K. M. Batoo, "X-ray peak profile analysis and optical properties of CdS nanoparticles synthesized via the hydrothermal method," *Applied Physics A: Materials Science & Processing*, vol. 125, no. 4, p. 283, 2019.

[52] T. C. Paul and J. Podder, "Synthesis and characterization of Zn-incorporated TiO_2 thin films: impact of crystallite size on X-ray line broadening and bandgap tuning," *Applied Physics A: Materials Science & Processing*, vol. 125, no. 12, p. 818, 2019.

[53] Q. Zhang, Z. Qin, Q. Luo et al., "Microstructure and nanoindentation behavior of Cu composites reinforced with graphene nanoplatelets by electroless co-deposition technique," *Scientific Reports*, vol. 7, no. 1, p. 1338, 2017.

[54] S. Debnath and R. Das, "Cobalt doping on nickel ferrite nanocrystals enhances the micro-structural and magnetic properties: shows a correlation between them," *Journal of Alloys and Compounds*, vol. 852, article 156884, 2021.

[55] V. Kumar, S. K. Singh, H. Sharma, S. Kumar, M. K. Banerjee, and A. Vij, "Investigation of structural and optical properties of ZnO thin films of different thickness grown by pulsed laser deposition method," *Physica B: Condensed Matter*, vol. 552, pp. 221–226, 2019.

[56] K. Kombaiah, J. J. Vijaya, L. J. Kennedy, and K. Kaviyarasu, "Catalytic studies of $NiFe_2O_4$ nanoparticles prepared by conventional and microwave combustion method," *Materials Chemistry and Physics*, vol. 221, pp. 11–28, 2019.

[57] M. Beyranvand and A. Gholizadeh, "Structural, magnetic, elastic and dielectric properties of $Mn_{0.3-x}$ Cd_x $Cu_{0.2}Zn_{0.5-}$ Fe_2O_4 nanoparticles," *Journal of Materials Science: Materials in Electronics*, vol. 31, pp. 5124–5140, 2020.

[58] F. Jelokhani, S. Sheibani, and A. Ataie, "Adsorption and photocatalytic characteristics of cobalt ferrite-reduced graphene oxide and cobalt ferrite-carbon nanotube nanocomposites," *Journal of Photochemistry and Photobiology A: Chemistry*, vol. 403, article 112867, 2020.

[59] J. Massoudi, M. Smari, K. Khirouni, E. Dhahri, and L. Bessais, "Impact of particle size on the structural and smagnetic properties of superparamagnetic Li-ferrite nanoparticles," *Journal of Magnetism and Magnetic Materials*, vol. 528, article 167806, 2021.

[60] J. Wang, Q. Deng, M. Li et al., "Copper ferrites@reduced graphene oxide anode materials for advanced lithium storage applications," *Scientific Reports*, vol. 7, no. 1, p. 8903, 2017.

[61] E. E. Ateia, R. Ramadan, and A. S. Shafaay, "Efficient treatment of lead-containing wastewater by $CoFe_2O_4$/ graphene nanocomposites," *Applied Physics A: Materials Science & Processing*, vol. 126, no. 3, p. 222, 2020.

[62] A. Nasiri, M. Nasiri, S. Nouhi, and S. Khodadadian, "Nanocrystalline copper ferrite: synthesis of different shapes through a new method and its photocatalyst application," *Journal of Materials Science: Materials in Electronics*, vol. 28, pp. 2401–2406, 2017.

[63] W. Wang and D. Zhang, "Facile preparation of rGO/MFe_2O_4(M = Cu, Co, Ni) nanohybrids and its catalytic performance during the thermal decomposition of ammonium perchlorate," *RSC Advances*, vol. 8, no. 56, pp. 32221–32230, 2018.

[64] Y. Fu, Q. Chen, M. He et al., "Copper ferrite-graphene hybrid: a multifunctional heteroarchitecture for photocatalysis and energy storage," *Industrial and Engineering Chemistry Research*, vol. 51, no. 36, pp. 11700–11709, 2012.

[65] P. T. L. Huong, N. Tu, H. Lan et al., "Functional manganese ferrite/graphene oxide nanocomposites: effects of graphene oxide on the adsorption mechanisms of organic MB dye and inorganic As(v) ions from aqueous solution," *RSC Advances*, vol. 8, no. 22, pp. 12376–12389, 2018.

[66] M. Zhu, D. Meng, C. Wang, and G. Diao, "Facile fabrication of hierarchically porous $CuFe_2O_4$ nanospheres with enhanced capacitance property," *ACS Applied Materials & Interfaces*, vol. 5, no. 13, pp. 6030–6037, 2013.

[67] A. G. Tabrizi, N. Arsalani, A. Mohammadi, H. Namazi, L. S. Ghadimi, and I. Ahadzadeh, "Facile synthesis of a $MnFe_2O_4$/rGO nanocomposite for an ultra-stable symmetric supercapacitor," *New Journal of Chemistry*, vol. 41, no. 12, pp. 4974–4984, 2017.

[68] L. Kong, Z. Li, X. Huang et al., "Efficient removal of Pb(ii) from water using magnetic Fe_3S_4/reduced graphene oxide composites," *Journal of Materials Chemistry A*, vol. 5, no. 36, pp. 19333–19342, 2017.

[69] N. Hussain, P. Gogoi, P. Khare, and M. R. Das, "Nickel nanoparticles supported on reduced graphene oxide sheets: a phosphine free, magnetically recoverable and cost effective catalyst for sonogashira cross-coupling reactions," *RSC Advances*, vol. 5, no. 125, pp. 103105–103115, 2015.

[70] M. Cao, L. Feng, P. Yang, H. Wang, X. Liang, and X. Chen, "Fabrication of reduced graphene oxide decorated with gold and nickel for the catalytic reduction of 4-nitrophenol," *Journal of Materials Science*, vol. 53, no. 7, pp. 4874–4883, 2017.

[71] M. A. M. Khan, W. Khan, M. Ahamed, J. Ahmed, M. A. al-Gawati, and A. N. Alhazaa, "Silver-decorated cobalt ferrite nanoparticles anchored onto the graphene sheets as electrode materials for electrochemical and photocatalytic applications," *ACS Omega*, vol. 5, no. 48, pp. 31076–31084, 2020.

[72] A. R. Kagdi, N. P. Solanki, F. E. Carvalho et al., "Influence of Mg substitution on structural, magnetic and dielectric properties of X-type bariumzinc hexaferrites Ba2Zn2-xMgxFe28O46," *Journal of Alloys and Compounds*, vol. 741, pp. 377–391, 2018.

[73] H. N. Chaudhari, P. N. Dhruv, C. Singh, S. S. Meena, S. Kavita, and R. B. Jotania, "Effect of heating temperature on structural, magnetic and dielectric properties of magnesium ferrites prepared in the presence of Solanum lycopersicum fruit extract," *Journal of Materials Science: Materials in Electronics*, vol. 31, no. 21, pp. 18445–18463, 2020.

[74] N. M. Mahmoodi, A. Taghizadeh, M. Taghizadeh, and M. A. S. Baglou, "Surface modified montmorillonite with cationic surfactants: preparation, characterization, and dye adsorption from aqueous solution," *Journal of Environmental Chemical Engineering*, vol. 7, no. 4, article 103243, 2019.

[75] S. S. M. Hassan, A. H. Kamel, M. A. Youssef, A. H. A. Aboterika, and N. S. Awwad, "Removal of barium and strontium from wastewater and radioactive wastes using a green bioadsorbent, Salvadora persica (Miswak)," *Desalination and Water Treatment*, vol. 192, pp. 306–314, 2020.

[76] J. Wei, M. F. Aly Aboud, I. Shakir, Z. Tong, and Y. Xu, "Graphene oxide-supported organo-montmorillonite composites for the removal of Pb(II), Cd(II) and As(v) contaminants from water," *ACS Applied Nano Materials*, vol. 3, no. 1, pp. 806–813, 2020.

[77] O. N. Collins and O. C. Elijah, "Adsorption of a dye (crystal violet) on an acid modified non-conventional adsorbent," *Journal of Chemical Technology & Metallurgy*, vol. 54, no. 1, pp. 95–110, 2019.

[78] B. M. Jafar, I. Hamadneh, F. I. Khalili, and A. H. Al-Dujaili, "Kinetic study on adsorption of fatty hydroxamic acids by natural clays," *Jordan Journal of Earth and Environmental Sciences*, vol. 7, no. 1, pp. 11–17, 2015.

[79] D. Lin, F. Wu, Y. Hu et al., "Adsorption of dye by waste black tea powder: parameters, kinetic, equilibrium, and thermodynamic studies," *Journal of Chemistry*, vol. 2020, Article ID 5431046, 13 pages, 2020.

[80] A. P. Vieira, S. A. A. Santana, C. W. B. Bezerra et al., "High performance maleated lignocellulose epicarp fibers for copper ion removal," *Brazilian Journal of Chemical Engineering*, vol. 31, no. 1, pp. 183–193, 2014.

[81] A. A. Inyinbor, F. A. Adekola, and G. A. Olatunji, "Kinetics and isothermal modeling of liquid phase adsorption of rhodamine B onto urea modified Raphia hookerie epicarp," *Applied Water Science*, vol. 7, no. 6, pp. 3257–3266, 2017.

[82] N. Kaur, M. Kaur, and D. Singh, "Fabrication of mesoporous nanocomposite of graphene oxide with magnesium ferrite for efficient sequestration of Ni (II) and Pb(II) ions: adsorption, thermodynamic and kinetic studies," *Environmental Pollution*, vol. 253, pp. 111–119, 2019.

[83] H. Li, L. Zhang, Z. Sun, Y. Liu, B. Yang, and S. Yan, "One-step synthesis of magnetic 1,6-hexanediamine-functionalized reduced graphene oxide-zinc ferrite for fast adsorption of Cr(vi)," *RSC Advances*, vol. 5, no. 40, pp. 31787–31797, 2015.

[84] M. D. Yahya, K. S. Obayomi, M. B. Abdulkadir, Y. A. Iyaka, and A. G. Olugbenga, "Characterization of cobalt ferrite-supported activated carbon for removal of chromium and lead ions from tannery wastewater via adsorption equilibrium," *Water Science and Engineering*, vol. 13, no. 3, pp. 202–213, 2020.

[85] O. K. Amadi, C. J. Odidiozor, and I. A. Okoro, "Sorption kinetic and intraparticle diffusivities of As^{3+} and Hg^{2+} detoxification from aqueous solution suing cellulosic biosorbent derived from okra (Abelmoschus esculentus) stems," *International Journal of Engineering and Information Systems*, vol. 1, no. 8, pp. 72–85, 2017.

[86] A. A. Babaei, Z. Alaee, E. Ahmadpour, and A. Ramazanpour-Esfahani, "Kinetic modeling of methylene blue adsorption onto acid-activated spent tea: a comparison between linear and non-linear regression analysis," *Journal of Advances in Environmental Health Research*, vol. 2, no. 4, pp. 197–208, 2014.

[87] A. Pholosi, E. B. Naidoo, and A. E. Ofomaja, "Intraparticle diffusion of Cr(VI) through biomass and magnetite coated biomass: a comparative kinetic and diffusion study," *South African Journal of Chemical Engineering*, vol. 32, pp. 39–55, 2020.

[88] Z. Falahian, F. Torki, and H. Faghihian, "Synthesis and application of polypyrrole/Fe_3O_4 nanosize magnetic adsorbent for efficient separation of Hg^{2+} from aqueous solution," *Global Challenges*, vol. 2, no. 1, article 1700078, 2018.

[89] F.-C. Wu, B.-L. Liu, K.-T. Wu, and R.-L. Tseng, "A new linear form analysis of Redlich-Peterson isotherm equation for the adsorptions of dyes," *Chemical Engineering Journal*, vol. 162, no. 1, pp. 21–27, 2010.

[90] P. T. L. Huong, L. T. Huy, V. N. Phan et al., "Application of graphene oxide- $MnFe_2O_4$ magnetic nanohybrids as magnetically separable adsorbent for highly efficient removal of arsenic from water," *Journal of Electronic Materials*, vol. 45, no. 5, pp. 2372–2380, 2016.

[91] J. A. Pellicer, M. I. Rodríguez-López, M. I. Fortea et al., "Adsorption properties of β- and hydroxypropyl-β-cyclodextrins cross-linked with epichlorohydrin in aqueous solution. A sustainable recycling strategy in textile dyeing process," *Polymers (Basel)*, vol. 11, no. 2, p. 252, 2019.

[92] N. Chung Le and D. Van Phuc, "Sorption of lead (II), cobalt (II) and copper (II) ions from aqueous solutions by γ- MnO_2 nanostructure," *Advances in Natural Sciences: Nanoscience and Nanotechnology*, vol. 6, article 025014, 2015.

[93] P. Zhao, M. Jian, R. Xu et al., "Removal of arsenic (III) from water by 2D zeolite imidazolate framework -67 nanosheets," *Environmental Science: Nano*, vol. 7, no. 11, pp. 3616–3626, 2020.

[94] Q. Li, R. Li, X. Ma et al., "Efficient removal of antimonate from water by yttrium-based metal-organic framework: adsorbent stability and adsorption mechanism investigation," *Colloids and Surfaces, A: Physiochemical and Engineering Aspects*, vol. 633, article 127877, 2022.

[95] H. Li, Y. Yao, J. Chen et al., "Heterogeneous activation of peroxymonosulfate by bimetallic MOFs for efficient degradation of phenanthrene: Synthesis, performance, kinetics, and mechanisms," *Separation and Purification Technology*, vol. 259, article 118217, 2021.

[96] H. T. Van, L. H. Nguyen, N. V. Dang et al., "The enhancement of reactive red 24 adsorption from aqueous solution using agricultural waste-derived biochar modified with ZnO nanoparticles," *RSC Advances*, vol. 11, no. 10, pp. 5801–5814, 2021.

[97] C. P. Wang, J. Z. Wu, H. W. Sun, T. Wang, H. B. Liu, and Y. Chang, "Adsorption of Pb(II) ion from aqueous solutions by tourmaline as a novel adsorbent," *Industrial and Engineering Chemistry Research*, vol. 50, no. 14, pp. 8515–8523, 2011.

[98] C. M. Park, Y. M. Kim, K. H. Kim, D. Wang, C. Su, and Y. Yoon, "Potential utility of graphene-based nano spinel ferrites as adsorbent and photocatalyst for removing organic/inorganic contaminants from aqueous solutions: a mini review," *Chemosphere*, vol. 221, pp. 392–402, 2019.

[99] Z. Mahdi, Q. J. Yu, and A. El Hanandeh, "Removal of lead (II) from aqueous solution using date seed-derived biochar: batch and column studies," *Applied Water Science*, vol. 8, no. 6, p. 181, 2018.

[100] K. Dai, G. Liu, W. Xu et al., "Judicious fabrication of bifunctionalized graphene oxide/$MnFe_2O_4$ magnetic nanohybrids

for enhanced removal of Pb(II) from water," *Journal of Colloid and Interface Science*, vol. 579, pp. 815–822, 2020.

[101] L. P. Lingamdinne, I.-S. Kim, J.-H. Ha, Y.-Y. Chang, J. R. Koduru, and J.-K. Yang, "Enhanced adsorption removal of Pb(II) and Cr(III) by using nickel ferrite-reduced graphene oxide nanocomposite," *Metals*, vol. 7, no. 6, p. 225, 2017.

[102] S. Kumar, R. R. Nair, P. B. Pillai, S. N. Gupta, M. A. Iyengar, and A. K. Sood, "Graphene oxide–$MnFe_2O_4$ magnetic nanohybrids for efficient removal of lead and arsenic from water," *ACS Applied Materials & Interfaces*, vol. 6, no. 20, pp. 17426–17436, 2014.

[103] N. V. Hao, N. V. Dang, D. H. Tung, P. T. Tan, N. V. Tu, and P. V. Trinh, "Facile synthesis of graphene oxide from graphite rods of recycled batteries by solution plasma exfoliation for removing Pb from water," *RSC Advances*, vol. 10, no. 67, pp. 41237–41247, 2020.

[104] S. Banerjee and M. C. Chattopadhyaya, "Adsorption characteristics for the removal of a toxic dye, tartrazine from aqueous solutions by a low cost agricultural by-product," *Arabian Journal of Chemistry*, vol. 10, no. 2, pp. S1629–S1638, 2017.